

# Numerical modeling of CO<sub>2</sub> fracturing by the phase field approach

Mostafa Mollaali<sup>a</sup>, Vahid Ziaei-Rad<sup>b</sup>, Yongxing Shen<sup>a,\*</sup>

<sup>a</sup> University of Michigan – Shanghai Jiao Tong University Joint Institute, Shanghai Jiao Tong University, Shanghai, 200240, China

<sup>b</sup> Department of Civil Engineering, Isfahan University of Technology, Isfahan, 84156-83111, Iran

## ARTICLE INFO

### Keywords:

CO<sub>2</sub> fracturing

CO<sub>2</sub> fluid flow

Phase field model

65K10



## ABSTRACT

We propose a phase field model to simulate CO<sub>2</sub> fracturing under an isothermal condition. We take advantage of the ability of the phase field approach in predicting fracture initiation and branching, and also to avoid tracking the fracture path. We model the CO<sub>2</sub> as a compressible fluid by modifying Darcy's law. In particular, we assume the permeability is correlated to the phase field value by an exponential function. The dependence of the CO<sub>2</sub> density as a function of the pressure is captured by the Span-Wagner equation of state. The computed breakdown pressure values show good agreement with analytical solutions and experimental results.

## 1. Introduction

Shale gas is the natural gas trapped within the shale, or mudstone reservoir. Shale is a fine-grained, sedimentary rock composed of clay minerals and silt-sized particles. The shale has low permeability so that it significantly inhibits the gas flow from the reservoir rocks to the production wells. As a result, the economic feasibility of shale gas development relies on the effective stimulation of the reservoirs (Hattori et al., 2017). Shale gas has become an energy source of increasing worldwide interest due to the two technologies that have become mature in industry: horizontal drilling and hydraulic fracturing technique (Middleton et al., 2014).

To date, water-based fluids are the most important fluids regularly used in the commercial shale gas due to their ready availability and low cost. But there are also some disadvantages to use water-based fluids, namely water shortage, contamination of underground water, and low fracturing performance. Also, hydraulic fracturing cannot avoid the clay swelling problem in shale (Middleton et al., 2014). Due to these problems, researchers actively investigate non-aqueous (see (Wang et al., 2016)) and non-fluid fracturing techniques such as explosive based method (Miller and Johansen, 1976).

Carbon dioxide (CO<sub>2</sub>) is one of the non-aqueous fracturing fluids that is considered to be used for fracturing. CO<sub>2</sub> as a fracturing fluid has been successfully applied to fracturing unconventional gas reservoirs decades ago (Lillies and King, 1982). Since the critical temperature of CO<sub>2</sub> is 31.1 °C, once the pressure exceeds its critical pressure of 7.38 MPa, it will change to the supercritical state (Suehiro et al., 1996). It can be injected down-hole either in liquid or supercritical state. The main benefits of CO<sub>2</sub> as a fracturing fluid include reducing consumption

of water and water contamination, keeping clays (smectite and illite) stabilized, and preventing metal leaching and chemical interactions.

Brown (2000) proposed CO<sub>2</sub> as a fracturing fluid and circulating fluid in geothermal energy extraction. Middleton et al. (2015) investigated the potential of using CO<sub>2</sub> as a fracturing fluid for commercial scale of shale production. In the laboratory scale, Ishida et al., 2012, 2016 conducted fracturing experiments by using supercritical CO<sub>2</sub>. Also, some researchers investigated the effect of different fracturing fluids (Wang et al., 2018; Zhou and Burbey, 2014).

There exist two general approaches for modeling fracture. One is discrete models for fracture where the geometrical discontinuity is modeled by modifying the geometry of intact structure (Ngo and Scordelis, 1967; Moës et al., 1999; Rangarajan et al., 2015; Verhoosel et al., 2011). The other is smeared crack models where the discontinuity is distributed over a finite width, such as the phase field (Bourdin et al., 2000) and the gradient-enhanced damage methods (Peerlings et al., 1996). In this approach, an additional unknown and a length scale are introduced.

Phase field modeling of fracture has gained popularity since the beginning of this century. The phase field model by Bourdin et al. (2000) is essentially a regularization of the variational formulation of brittle fracture by Francfort and Marigo (1998). What makes the phase field an attractive approach can be attributed to its convenience in simulating complex fracture processes, including crack initiation, propagation, branching and merging. Compared to discrete fracture descriptions, the phase field approaches avoid tracking the complicated crack geometry; instead, the crack evolution is a natural outcome of the numerical solution to a constrained optimization problem. Thus, it significantly decreases the implementation difficulty, especially when

\* Corresponding author.

E-mail address: [yongxing.shen@sjtu.edu.cn](mailto:yongxing.shen@sjtu.edu.cn) (Y. Shen).

<https://doi.org/10.1016/j.jngse.2019.102905>

Received 27 October 2018; Received in revised form 10 May 2019; Accepted 1 June 2019

Available online 15 June 2019

1875-5100/ © 2019 Elsevier B.V. All rights reserved.

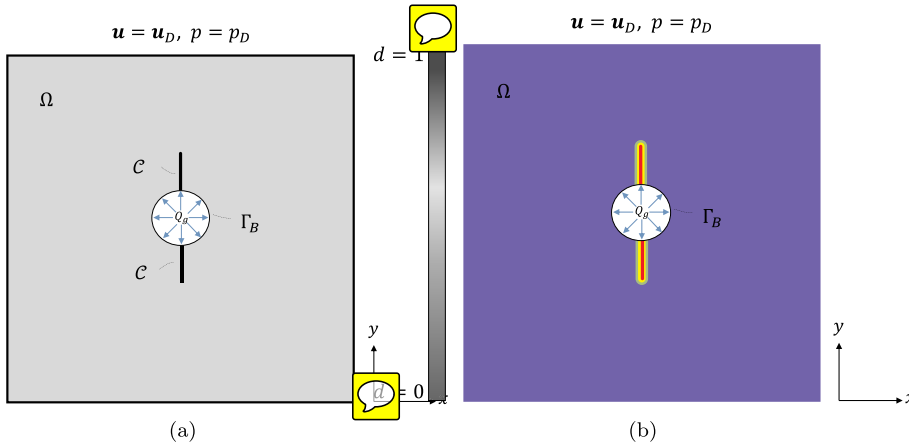


Fig. 1. Schematic of (a) a sharp fracture and (b) the diffusive phase field profile for the same fracture. In both figures, a square plate with a borehole placed inside is shown. The *in situ* stress is applied on the external boundary, while the fluid is injected from the boundary of the borehole. We will only use the diffusive phase field in the proposed method.

dealing with 3D problems.

Bourdin et al. (2012) have adopted the phase field approach to model hydraulic fracturing in impermeable media by considering the force that fluid pressure exerts on fracture surfaces. Afterwards, phase field approaches for hydraulic fracture in porous media based on Biot's equations and the theory of porous media have been investigated by many researchers.

Mikelić et al. (2014) model pressurized fracture in porous media by combining the Biot theory and phase field approach. To minimize code modifications for adopting the phase field approach with an existing reservoir simulator, Yoshioka and Bourdin (2016) have proposed an efficient framework by modifying the Darcy law. Wick et al. (2016) have developed a model to simulate fluid-filled fracture propagation coupled to a reservoir simulator. Also, they have used a single pressure equation for the entire fractured domain by introducing a function to distinguish between reservoir and fracture domains. Mauthe and Miehe (2017) have coupled the phase field hydraulic fracture and porous media fluid flow by using a permeability decomposition. Ehlers and Luo (2017) have combined the theory of porous media (TPM) and the phase field approach to fracture. Also, Culp et al. (2017) have applied the phase field approach to fracture in CO<sub>2</sub> sequestration. In most cases researchers have supposed the fracturing fluid is incompressible or slightly compressible. Recently, Heider and Markert (2017) proposed a method to model the pore fluid which is considered compressible.

The objective of the paper at hand is to propose a phase field model to investigate the effect of CO<sub>2</sub> as a compressible fracturing fluid under the isothermal condition, as the first step towards such modeling. For this purpose, we have adopted the phase field approach to model fracturing in porous media according to Mikelić et al. (2014). We model the CO<sub>2</sub> flow as a compressible fluid by modifying Darcy's law. We suppose permeability is correlated to the phase field value by an exponential function. The CO<sub>2</sub> density varies significantly with pressure, which is captured by the Span-Wagner equation of state (Span and Wagner, 1996).

In the remaining paper we will proceed as follows: a description of the fracture problem is given in Section 2, including the governing equations of the solid and the fluid flow. Afterwards, the numerical discretization and algorithm are constructed in Section 3. Then Section 4 provides numerical examples and discussions, where we will show

that our results for the breakdown pressure agree well with not only widely used analytical solutions but also, within a reasonable error, with experimental results. Finally Section 5 draws conclusions.

## 2. Mathematical model

This section describes the mathematical model we will adopt for CO<sub>2</sub> fracturing. For convenience we will confine ourselves to the two-dimensional plane strain case, but the formulation is applicable to three dimensions with minimal changes. During the CO<sub>2</sub> fracturing process, the gas penetrates into the rock around the borehole and the injecting pressure causes the fracture to propagate. Thus, fracture propagation is a coupled phenomenon involving the gas flow inside the fracture and in the entire porous medium, the rock deformation, and the fracture propagation in the rock mass. In the following, in Section 2.1 we introduce the phase field method for fracture and derive the governing equations for the deformation and fracture propagation in the porous medium. Then, in Section 2.2 we present the governing equations for the gas flow within the porous medium. It is worth mentioning that compressible CO<sub>2</sub> exhibits a transport behavior different from that of slightly compressible fluids such as water and oil, due to its large compressibility and possibility of phase change.

### 2.1. Porous medium deformation and fracture propagation

In this section, we briefly recapitulate the basic notations and the underlying equations of the phase field method for pressurized fractures in brittle materials.

#### 2.1.1. Variational formulation of brittle fracture

We consider a two-dimensional porous medium under plane strain loading occupying an open Lipschitz domain (see Fig. 1a)  $\Omega \subset \mathbb{R}^2$ . Let  $\Gamma_D, \Gamma_N \subseteq \partial\Omega$  be such that  $\Gamma_D \cup \Gamma_N = \partial\Omega$  and  $\Gamma_D \cap \Gamma_N = \emptyset$ , and  $\mathbf{u}_D: \Gamma_D \rightarrow \mathbb{R}^2$  and  $\mathbf{t}_N: \Gamma_N \rightarrow \mathbb{R}^2$  be prescribed displacement and traction boundary conditions, respectively. Also, let  $\Gamma_B \subset \partial\Omega$  denote the boundary of a borehole. We let  $q_B: \Gamma_B \rightarrow \mathbb{R}$  denote the fluid source and  $\mathbf{b}: \Omega \rightarrow \mathbb{R}^2$  the body force per unit volume exerted to the solid.

The variational approach to fracture is built on energy minimization with respect to the displacement field  $\mathbf{u}: \Omega \rightarrow \mathbb{R}^2$  and its jump set, which

we denote as  $\mathcal{C} = \mathcal{C}(\mathbf{u}) \subset \Omega$ . Let  $|\mathcal{C}|$  denote the one-dimensional Hausdorff measure of  $\mathcal{C}$ . Following Griffith's theory, the total potential energy of the fractured poroelastic solid is written as:

$$\begin{aligned} \Pi_{\mathcal{C}}[\mathbf{u}, \mathcal{C}] &= \int_{\Omega \setminus \mathcal{C}} \psi_0[\varepsilon(\mathbf{u})] d\Omega - \int_{\Omega} \mathbf{b} \cdot \mathbf{u} d\Omega - \int_{\Gamma_N} \mathbf{t}_N \cdot \mathbf{u} d\Gamma \\ &- \int_{\Omega \setminus \mathcal{C}} (\alpha - 1)p \operatorname{div} \mathbf{u} d\Omega + \int_{\Omega \setminus \mathcal{C}} \nabla p \cdot \mathbf{u} d\Omega + g_c |\mathcal{C}|, \end{aligned} \quad (1)$$

where  $p$  denotes the pore pressure,  $\alpha \in [0, 1]$  is the Biot coefficient. Constant  $g_c \in \mathbb{R}^+$  is the strain energy released per unit length of fracture extension. The strain energy density  $\psi_0[\varepsilon(\mathbf{u})]$  is given by

$$\psi_0(\varepsilon) = \frac{\lambda}{2} (\operatorname{tr} \varepsilon)^2 + G \|\varepsilon\|^2,$$

with  $\lambda$  and  $G$  Lamé constants. These constants are related to Young's modulus  $E$  and Poisson's ratio  $\nu$  as  $\lambda = E\nu/[(1 + \nu)(1 - 2\nu)]$  and  $G = E/[2(1 + \nu)]$ . The linearized strain tensor takes the form:

$$\varepsilon(\mathbf{u}) = \frac{1}{2} (\nabla \mathbf{u} + \nabla \mathbf{u}^T).$$

Finally,  $\|\cdot\|$  denotes the Frobenius norm of a tensor.

### 2.1.2. Regularized variational formulation of brittle fracture

To develop a numerical method to approximate (1), the phase field approach replaces the sharp-fracture description  $\mathcal{C}$  with a phase field description (see Fig. 1b), where the phase field is denoted as  $d: \Omega \rightarrow [0, 1]$ . In particular, regions with  $d = 0$  and  $d = 1$  correspond to the intact and fully broken materials, respectively. Using a phase field approach, the one-dimensional fracture  $\mathcal{C}$  is approximated with the help of an elliptic functional (Ambrosio and Tortorelli, 1990, 1992):

$$\mathcal{C}_{\ell}[d] = \frac{1}{4c_w} \int_{\Omega} \left( \frac{w(d)}{\ell} + \ell \nabla d \cdot \nabla d \right) d\Omega, \quad (2)$$

where  $\ell > 0$  is the regularization length scale, which may also be interpreted as a material property, e.g., the size of the process zone. See Remark 3 for comments on the choice of  $\ell$ . Constant  $c_w = \int_0^1 \sqrt{w(d)} d$  is a normalization constant such that when  $\ell \rightarrow 0$ ,  $\mathcal{C}_{\ell}[d]$  converges to the length of the sharp fracture,  $|\mathcal{C}|$ . Classical examples of  $w(d)$  and  $c_w$  are  $w(d) = d^2$  and  $c_w = 1/2$  for the AT2 model, and  $w(d) = d$  and  $c_w = 2/3$  for the AT1 model. Between these models, the AT1 model which is better at simulating crack nucleation (Tanné et al., 2018) predicts a phase field profile with a support of a finite width, but requires solving inequality constrained optimization problems; the AT2 model, which normally requires a pre-existing crack (at least for a homogeneous material under low-speed loading), gives a diffuse phase field profile, but the resulting equations are much easier to solve. Interested readers are referred to (Tanné et al., 2018; Bourdin et al., 2014) for more elaborations. In this paper all numerical examples are implemented with the AT1 model, while we keep our formulation general for both models.

On this basis, we replace (1) by a global constitutive dissipation functional for a rate independent fracture process (Bourdin et al., 2013):

$$\begin{aligned} \Pi[\mathbf{u}, d] &= \int_{\Omega} \psi[\varepsilon(\mathbf{u}), d] d\Omega - \int_{\Omega} \mathbf{b} \cdot \mathbf{u} d\Omega - \int_{\Gamma_N} \mathbf{t}_N \cdot \mathbf{u} d\Gamma \\ &- \int_{\Omega} (1 - d)^2 (\alpha - 1)p \operatorname{div} \mathbf{u} d\Omega + \int_{\Omega} (1 - d)^2 \nabla p \cdot \mathbf{u} d\Omega \\ &+ \frac{g_c}{4c_w} \int_{\Omega} \left( \frac{w(d)}{\ell} + \ell \nabla d \cdot \nabla d \right) d\Omega, \end{aligned} \quad (3)$$

where the admissible sets of displacement and phase field can be set as:

$$\mathcal{U}_u = \{\mathbf{u} \in H^1(\Omega; \mathbb{R}^2) | \mathbf{u} = \mathbf{u}_D \text{ on } \Gamma_D\}, \quad (4a)$$

$$\mathcal{U}_d = \{d \in H^1(\Omega) | 0 \leq d \leq 1\}. \quad (4b)$$

In practice, (4b) will be used in combination with the irreversibility constraint, to be elaborated in Remark 2.

**Remark 1.** (Strain energy degradation). The solid endures partial loss of stiffness due to the presence of fractures. In order to model this effect, the strain energy density is degraded with respect to the evolution of the phase field. Also note that as the damaged material responds differently to tension and compression, we let only a part of the strain energy density be degraded. For this purpose, we let the degraded strain energy in (3) take the following general form:

$$\psi(\varepsilon, d) = g(d)\psi_+ + \psi_-$$

where  $g(d)$  satisfies  $g(0) = 1$ ,  $g(1) = 0$ , and  $g'(d) < 0$  for all  $d$  such that  $0 \leq d \leq 1$  (Bourdin et al., 2000). A usual choice is  $g(d) = (1 - d)^2$ . On the other hand,  $\psi_{\pm} \geq 0$  are such that

$$\psi_+(\varepsilon) + \psi_-(\varepsilon) = \psi_0(\varepsilon).$$

Now since  $\partial\psi/\partial d = g'(d)\psi_+$ , only  $\psi_+$  contributes to fracture propagation.

There are several phase field models that differ in their choice of  $\psi_{\pm}$ . In this paper, we adopt the one proposed by Amor et al. (2009). This model assumes both volumetric expansion and deviatoric deformation contribute to fracture propagation, but volumetric compression does not. A decomposition of  $\varepsilon$  into volumetric and deviatoric parts reads:

$$\operatorname{vol} \varepsilon = \frac{1}{3} (\operatorname{tr} \varepsilon) \mathbf{1}, \quad \operatorname{dev} \varepsilon = \varepsilon - \operatorname{vol} \varepsilon.$$

See Appendix A.1 for more details.

**Remark 2.** (Irreversibility constraint). The requirement  $g'(d) < 0$  comes from the underlying irreversibility condition (the fracture can never heal) in time:

$$\partial_t d \geq 0. \quad (5)$$

Consequently, modeling of fracture evolution problems leads to inequality constraints, and sometimes gives rise to a variational inequality formulation.

As an alternative way to model the irreversibility, Miehe et al. (2010a) proposed a phase field model based on a local history field. In this model, the evolution of the phase field  $d$  is driven by the historically maximum value of  $\psi_+$  at the point of interest.

**Remark 3.** (The choice of  $\ell$ ). Based on an analytical solution for the critical tensile strength  $\sigma_{cr}$  that a one-dimensional bar can sustain (Bourdin et al., 2014), we use the following equation for the choice of  $\ell$ :

$$\ell = \frac{3Eg_c}{8\sigma_{cr}^2}, \quad (6)$$

where  $E$  and  $g_c$  can be obtained from regular experiments, while  $\sigma_{cr}$  can be approximated by the tensile strength  $\sigma_T$ . Assuming all other parameters are known, formula (6) is able to estimate  $\ell$ , though more investigation is recommended for more complex cases.

### 2.2. Carbon dioxide as a compressible fluid

The governing equations for the fluid flow in a porous medium are given by mass conservation, momentum balance, and the equation of state. The mass conservation equation reads:

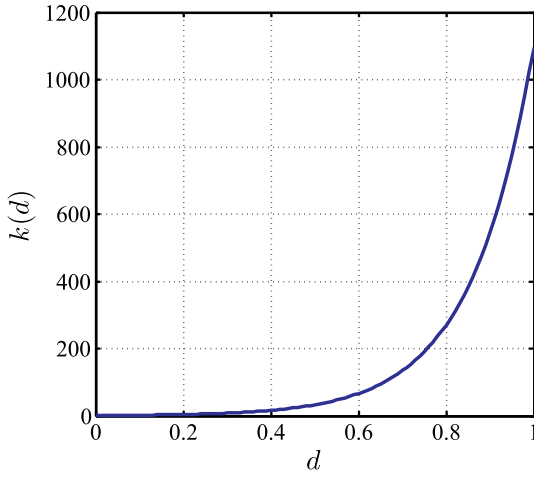


Fig. 2. Plot of  $k(d) = \exp(7.0d)$ , permeability, as a function of the phase field variable  $d$ .

$$\begin{aligned} \partial_t(\varphi\rho) + \nabla \cdot (\rho\mathbf{v}) &= 0 \quad \text{in } \Omega, \\ -\rho\mathbf{v} \cdot \mathbf{n} &= Q_g \quad \text{on } \Gamma_B. \end{aligned} \quad (7)$$

Here  $\varphi$  denotes the porosity of the porous medium (the fraction of volume occupied by the fluid),  $\rho$  the density of the fluid,  $\mathbf{v}$  the Darcy velocity vector, and  $Q_g$  the fluid source. Note that  $Q_g$  has the unit of volumetric flow rate per unit volume. Also, we assume the rock is saturated by the fluid so that the fluid content in rock per volume is expressed by  $\varphi\rho$ .

In addition to (7), we state the momentum balance in the form of Darcy's law. Note that this assumption is for the flow in conventional reservoirs, although there are more complicated flow regimes, namely slip flow, transition flow, and Knudsen diffusion, for which Darcy's law in its current form cannot be used. For more details we refer the reader to (Javadpour et al., 2007; Javadpour, 2009; Hosseini et al., 2015; Civan, 2010). Nevertheless modeling the flow at the microscale is out of the scope of this paper that deals with a continuum formulation, and hence we confine ourselves to Darcy's law throughout this work. This implies a linear relationship between the fluid velocity and the head pressure gradient:

$$\mathbf{v} = -\frac{k}{\mu} \nabla p, \quad (8)$$

where  $k = k(d)$  is the permeability of the rock, and  $\mu$  is the dynamic fluid viscosity. Note that there could be an additional term  $-\rho g \nabla z$  on the right hand side of (8), where  $g$  and  $z$  are the magnitude of the gravitational acceleration and the depth, respectively. This term is, however, in our case negligible, as we assume an almost horizontal computational domain. Also, we assume the porosity is not dependent on the stress condition.

On the other hand, we correlate the permeability to the phase field value as it is clear that when the crack starts propagating, the permeability of the solid matrix starts to increase, as the crack width increases. To incorporate this effect into our model, an exponential variation of the fluid permeability has been adopted from (Pillai et al., 2018; Zhu et al., 2013):

$$k(d) = k_0 \exp(\alpha_k d), \quad (9)$$

where  $k_0$  is the permeability of the intact material, and  $\alpha_k$  is a coefficient to indicate the effect of phase field evolution on the permeability.

We take  $\alpha_k = 7.0$  according to (Zhu et al., 2013). In real applications,  $\alpha_k$  can be obtained from experiments. Fig. 2 illustrates the permeability increasing with respect to the evolution of the phase field variable. As seen therein, the permeability starts from an initial value for a completely intact porous medium to a very big value of permeability in the fully broken area.

The first term on the left hand side of (7), the rate of change of fluid content, can be written as:

$$\partial_t(\phi\rho) = \rho \partial_t \phi + \phi \partial_t \rho = \rho \partial_t \varepsilon_v + \phi \partial_t \rho, \quad (10)$$

where we have assumed the rate of change of pore volume is equal to that of the volumetric strain, which is given by  $\varepsilon_v = \nabla \cdot \mathbf{u}$ .

Under isothermal conditions, the gas density varies significantly with pressure. This is captured by an equation of state (EOS). One applicable EOS for CO<sub>2</sub> is known as the Span-Wagner (S-W) equation (Span and Wagner, 1996) defined in terms of the Helmholtz free energy. The CO<sub>2</sub> density and pressure are related by:

$$p = (1 + \delta\varphi_\delta')\rho RT, \quad (11)$$

where  $R$  is the universal gas constant, and  $\varphi_\delta'$  is the derivative of the residual part of the full expression of Helmholtz energy  $\varphi^r$  with respect to the reduced density  $\delta$ , with

$$\begin{aligned} \varphi^r(\delta, \tau) &= \sum_{i=1}^7 n_i \delta^{d_i} \tau^{t_i} + \sum_{i=8}^{34} n_i \delta^{d_i} \tau^{t_i} e^{-\delta^{c_i}} + \sum_{i=35}^{39} n_i \delta^{d_i} \tau^{t_i} e^{-\alpha_i (\delta - s_i)^2 - \beta_i (\tau - \eta_i)^2} \\ &\quad + \sum_{i=40}^{42} n_i \Delta^{b_i} \delta e^{C_i (\delta - 1)^2 - D_i (\tau - 1)^2}, \end{aligned} \quad (12)$$

in which

$$\Delta = \left\{ (1 - \tau) + A_i [(\delta - 1)^2]^{\frac{1}{2\beta_i}} \right\}^2 + B_i [(\delta - 1)^2]^{\alpha_i}.$$

In (12),  $\rho_c$  and  $T_c$  are the critical density and temperature, respectively, and  $\delta = \rho/\rho_c$  and  $\tau = T/T_c$  are the reduced ones. For the sake of brevity, here we do not provide the definitions and values of other parameters in (12), but refer the readers to (Span and Wagner, 1996).

By substituting (8), (9), (10), and (11) in (7), the governing equation for CO<sub>2</sub> flow is written as follows:

$$\begin{aligned} \varphi \partial_t \rho + \rho \partial_t \varepsilon_v - \nabla \cdot \left( \rho \frac{k(d)}{\mu} \nabla p \right) &= 0, \quad \text{in } \Omega, \\ \rho \mathbf{v} \cdot \mathbf{n} &= -Q_g, \quad \text{on } \Gamma_B, \\ p &= p_D, \quad \text{on } \Gamma_P, \end{aligned} \quad (13)$$

where  $\Gamma_P = \partial\Omega \setminus \Gamma_B$ .

**Summary of governing equations.** The governing equations for modeling the CO<sub>2</sub> fracturing are summarized as follows: for the porous medium deformation, the functional defined in (3) is minimized among  $(\mathbf{u}, d) \in \mathcal{S}_u \times \mathcal{S}_d$  under the constraint (5), while for the compressible fluid the boundary value problem (13) is used to solve for the pressure  $p$ .

**Advantages and limitations of the method.** The main advantage of the current approach is its convenience in simulating complex fracture processes, including crack initiation, propagation and merging. In fact, the evolution of fracture surfaces is the natural outcome of the solution of a coupled system of partial differential equations. Such a model significantly decreases the implementation difficulty by avoiding tracking the fracture geometry. In this work, taking advantage of the phase field approach, we consider CO<sub>2</sub> as a compressible fracturing fluid under an isothermal condition. Nevertheless, as this work is the first of its kind, herein a relatively simple model is used for the

calculation of gas flow and permeability in shale media.

### 3. Numerical solution

In this section we present an algorithm that adopts standard procedures to obtain a numerical method to solve the initial boundary value problem presented in Section 2. In this algorithm, a staggered approach is employed to solve the underlying equations, i.e., the solution is obtained via iteration between the variables (Bourdin et al., 2000, 2008). This idea is based on the fact that by fixing two variables, the problem becomes convex in the remaining unknown. However, one drawback for such an approach is that it might need many iterations to achieve convergence among the three fields.

For the problem at hand, we need to solve a coupled system consisting of mass balance for the compressible fluid and a dissipative potential energy with the phase field. We provide a fully iterative approach in which at each stage we solve for one unknown while the other two variables are fixed to their values at the last iteration. Readers are referred to Algorithm 1 for complete elaboration. An alternative algorithm is the fixed-stress split, see (Chukwudozie, 2016; Mikelić and Wheeler, 2013).

**Algorithm 1.** Algorithm for modeling the CO<sub>2</sub> by phase field.

```

Input:  $p_0, d_0, u_0, \rho_0$ , and  $\varepsilon_{tol}$ 
Output:  $p_n, d_n$ , and  $u_n, n = 1, \dots, N$ 
1 Set flow and mechanical boundary conditions  $\sigma_1, \sigma_3$ , and  $Q_g$ ;
2 for  $n = 1$  to  $N$ ; do
3   Set  $t = n\Delta t$  and  $k = 0$ ; /*  $k$  is an iteration counter */
4   repeat
5      $m = 0$ ; /*  $m$  is another iteration counter */
6     repeat
7       Step - P: compute  $p_n$  with (A.6);
8       Step - U: compute  $u_n$  with (A.1);
9       Update  $\rho_n^{(k+1)} \leftarrow \rho(p_n^{(k)})$  with (11);
10       $k + 1 \leftarrow k$ 
11    until  $\|p_n^{(k)} - p_n^{(k-1)}\|_2 < \varepsilon_{tol}$  and  $\|u_n^{(k)} - u_n^{(k-1)}\|_2 < \varepsilon_{tol}$ ;
12    Step - d: compute  $d_n$  with (A.1);
13     $m + 1 \leftarrow m$ 
14  until  $\varepsilon_d = \|d_n^{(m)} - d_n^{(m-1)}\|_2 < \varepsilon_{tol}$ ;
15   $u_{n-1} \leftarrow u_n$ ;
16   $p_{n-1} \leftarrow p_n$ ;
17   $\rho_{n-1} \leftarrow \rho_n$ ;
18 end

```

We implement our method on FEniCS, an open-source finite element software (Logg et al., 2012, pp. 173–225). Therein, the user merely needs to provide the variational form of the problem as well as the geometry and mesh information. Then, a big advantage of FEniCS is that the software itself completes all steps toward generating the global stiffness matrix.

Below we show an excerpt of the used FEniCS code. This piece of code performs some calculations for line 8 in Algorithm 1 wherein  $u$  is solved for while the other two unknowns are fixed. It first defines  $\varepsilon$ , and  $\psi(\varepsilon, d)$  in lines 1, 3, and 5, respectively. Then, the standard finite element shape functions are defined in line 8, and the admissible function space (TrialFunction), the test function space (TestFunction), and the unknown function  $u$  (Function) are defined in line 9. Afterwards, the elastic energy is introduced as a variational form in line 11. Finally, in lines 12 and 13, the code takes the first variation  $\delta\Pi[(u, d); \bar{u}]$  (A.1a) and the second variation  $\delta^2\Pi[(u, d); \bar{u}; \delta u]$  (A.2a) and builds the nodal residual vector as Residual\_u and the tangent stiffness matrix as Jacobian\_u.

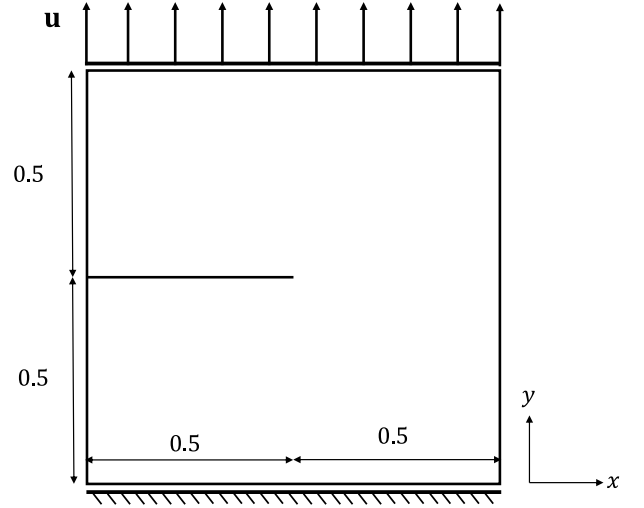


**Fig. 3.** Schematic of a cracked square plate (unit: mm) under a single-edge-notched tension test. A monotonically increasing displacement with constant increments  $\Delta u = 6 \times 10^{-5}$  mm is applied on the top edge while the bottom edge is fixed.

**Table 1**

Cracked square plate under a tension test: Material parameters (Ambati et al., 2015).

Parameters	symbol	unit	value
Young's modulus	$E$	MPa	$210 \times 10^3$
Poisson's ratio	$\nu$	—	0.3
Critical energy release rate	$g_c$	MPa mm	2.7

```

1 def eps(u_):
2   return sym(grad(u_))
3 def psi_0(u_):
4   return 0.5 * lmbda * tr(eps(u_))**2 + mu * eps(u_)**2
5 def psi(u_, d_):
6   return ((1 - d_)**2 + k_ell) * psi_0(u_)
7
8 V_u = VectorFunctionSpace(mesh, "CG", 1)
9 u_, u, u_t = Function(V_u), TrialFunction(V_u), TestFunction(V_u)
10
11 energy_elastic = psi(u_, d_) * dx
12 Residual_u = derivative(energy_elastic, u, u_t)
13 Jacobian_u = derivative(Residual_u, u, u_t)

```

To solve the three unknowns, we select for  $u$  and  $p$  the linear solver MUMPS which is convenient for solving large linear systems (Amestoy et al., 2000), and for  $d$  the TAO optimization solver integrated into the PETSc library (Munson et al., 2014; Balay et al., 2018), which has the capability of solving inequality constrained optimization problems as the one at hand. Interested readers are referred to (Bilgen et al., 2018) for more information about the applied solvers.

### 4. Numerical examples

In this section, we present a set of numerical examples to demonstrate the capability of the proposed model. First, we aim to verify our implementation of the present phase field method for CO<sub>2</sub> fracturing. To this end, we present three examples with exact or otherwise well-established solutions to verify our outputs. Next, we present three more numerical examples to demonstrate the capability of the proposed



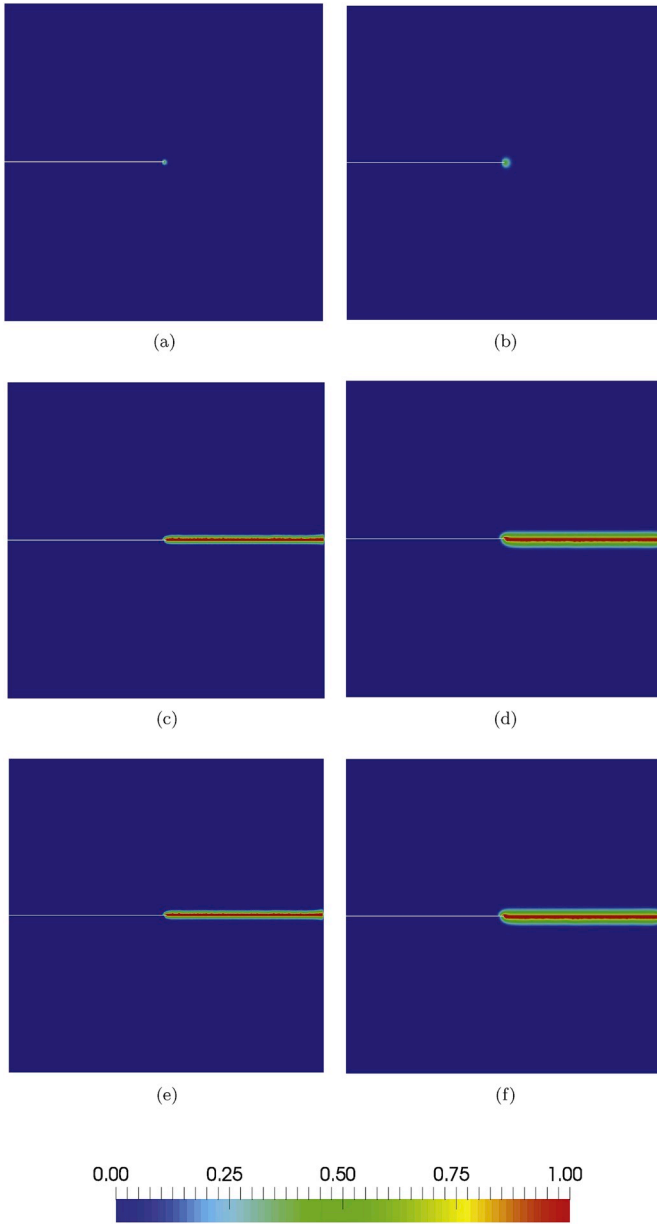


**Fig. 4.** Cracked square plate under a tension test with two different regularization length scales  $\ell = \ell_1 = 10^{-2}$  mm  $\approx 2h$  (left) and  $\ell = \ell_2 = 2 \times 10^{-2}$  mm  $\approx 4h$  (right). Both simulations are done with 100 uniform time steps with  $\Delta u = 6 \times 10^{-5}$  mm (See also Table 1 for the input values). Phase field contours at three different stages  $u = 5.52 \times 10^{-3}$  mm (4a,4b),  $u = 5.58 \times 10^{-3}$  mm (4c,4d), and  $u = 6 \times 10^{-3}$  mm (4e, 4f) are shown in deformed configurations with the deformations scaled. The initial cracks are explicitly imposed, so in the deformed configuration it appears as a white line. As expected, we observe a straight crack pattern in both cases.

model.

We also refer the interested readers to [Wilson and Landis \(2016\)](#) and [Chukwudozie \(2016\)](#) in which the phase field approach to hydraulic fracturing is verified with classical two-dimensional analytical solutions ([Detournay and Garagash, 2003](#); [Hu and Garagash, 2010](#)).

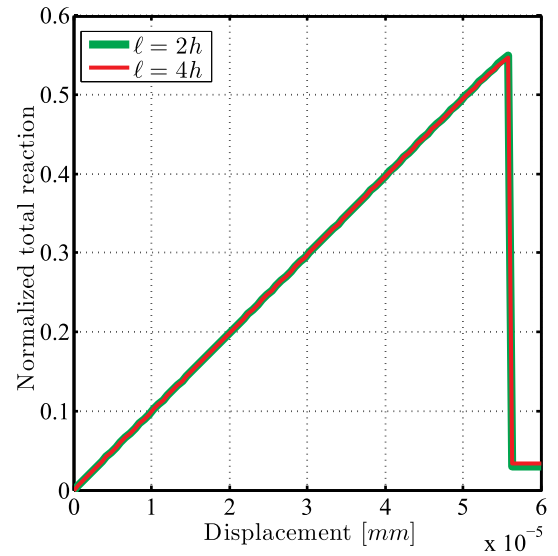


**Fig. 5.** Cracked square plate under a tension test with two different regularization length scales  $\ell = \ell_1 = 10^{-2}$  mm  $\approx 2h$  (red) and  $\ell = \ell_2 = 2 \times 10^{-2}$  mm  $\approx 4h$  (green). Load-deflection curves for both  $\ell_1$  and  $\ell_2$  are obtained. Both simulations are done with 100 load steps with  $\Delta u = 6 \times 10^{-5}$  mm. The total reaction is normalized by the one in the case without any crack or phase field evolution. Both models give rise to similar trends so the effect of changes in  $\ell$  is small within this range. Note that the reaction highly decreases at the 93rd time step where the crack starts to propagate.

**Table 2**

Poroelastic response of a borehole: Material parameters.

Parameters	symbol	unit	value
Young's modulus	$E$	MPa	6000
Poisson's ratio	$\nu$	—	0.34
Biot coefficient	$\alpha$	—	1.
Permeability	$k_0$	mm <sup>2</sup>	$1 \times 10^{-12}$

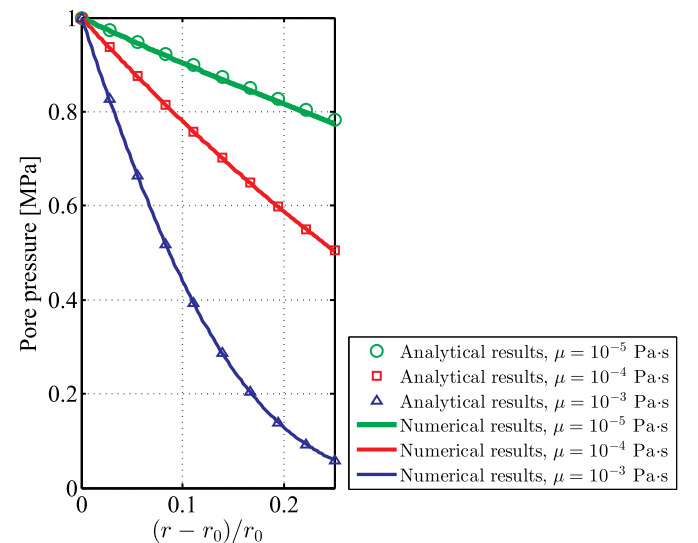


**Fig. 6.** Poroelastic response of a borehole. The distribution of pore pressure caused by fluid pressurization is shown around the borehole for three different dynamic viscosities  $\mu$  at early time  $t = 0.1$  s. As seen, the results are in good accordance with the analytical in ([Detournay and Cheng, 1988](#)).

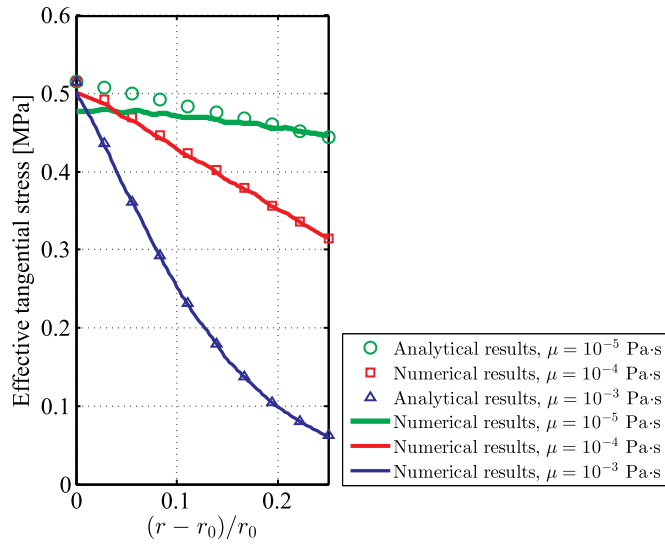


Fig. 7. Poroelastic response of a borehole. The effective tangential stress is plotted near the borehole for three different dynamic viscosities  $\mu$  at early time  $t = 0.1$  s.

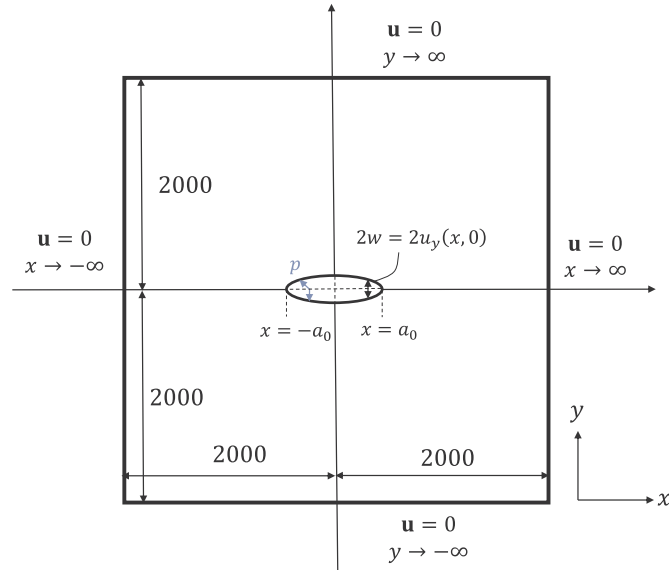


Fig. 8. Computation of the crack opening displacement. Schematic view of the deformed line crack in a two dimensional domain.

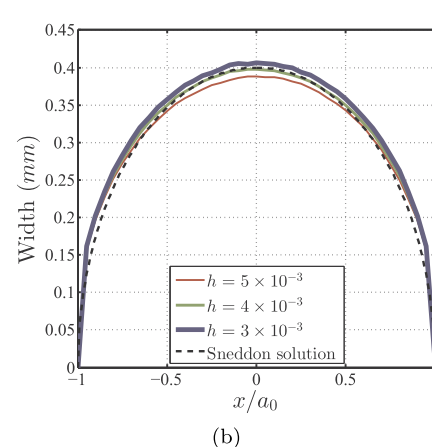
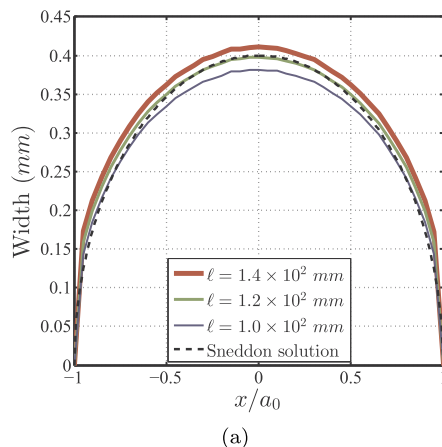


Fig. 9. Computation of the crack opening displacement. We output the results for (9a) various  $\ell$  with  $h = 4$  mm and (9b) various  $h$  with  $\ell = 1.2 \times 10^2$  mm, and compare them with Sneddon's analytical solution (Sneddon and Lowengrub, 1969).

Table 3

Crack volumes for different  $\ell$  for numerical tests and analytical solution ( $h = 4$  mm).

$\ell$ (mm)	$1.4 \times 10^2$	$1.2 \times 10^2$	$1.0 \times 10^2$
Numerical fracture volume (mm <sup>2</sup> )	$2.89 \times 10^2$	$2.75 \times 10^2$	$2.60 \times 10^2$
Analytical fracture volume (mm <sup>2</sup> )	$2.51 \times 10^2$		

#### 4.1. Single-edge-notched tension test

First, following an example motivated by Mische et al. (2010b), we investigate a square plate with a horizontal initial crack at the middle height starting from the left end and ending at the plate center. The geometric setup is depicted in Fig. 3. To capture the crack pattern properly, the mesh is refined in areas where the crack is expected to propagate, i.e., in the center strip of the specimen. In effect, for a discretization with 105,352 standard  $P_1$  elements, an effective element size of  $h \approx 5 \times 10^{-3}$  mm is obtained in the critical zone. The specimen is under a direct tension test, in which a monotonically increasing displacement with constant increments  $\Delta u = 6 \times 10^{-5}$  mm is imposed on the top edge while the bottom edge is fixed. In this example, the evolution is simulated for 100 uniform time steps so that a final deformation of  $6 \times 10^{-3}$  mm is reached. We will adopt the values of the material parameters given in Table 1.

The resulting crack patterns at different stages of the deformation for two fixed regularization length scales  $\ell = \ell_1 = 1 \times 10^{-2}$  mm and  $\ell = \ell_2 = 2 \times 10^{-2}$  mm are illustrated in Fig. 4. As expected, in both simulations, the fracture propagates straightforward to the end. This straight crack topology agrees well with the results in (Mische et al., 2010c). Also as seen, the resulting crack pattern with the smaller  $\ell$  looks sharper.

We also output the load-deflection curves for the two setups of Fig. 5. As seen, both models will result in similar trends. Hence, the effect of  $\ell$  on the response is small in this range.

#### 4.2. Poroelastic response of a borehole

This example aims to study the effect of fluid pressurization on the poroelastic response around the borehole. It was first studied by Detournay and Cheng (Detournay and Cheng, 1988) (see also (Wang et al., 2018; Lu et al., 2013)). Consider a plane strain hydraulic fracturing problem where there is a square plate containing a central borehole. The geometry and the loading conditions in this example are the same as Fig. 12. The far-field *in situ* stress is set to zero in this example. Note also that  $d \equiv 0$ , i.e., there is no pre-existing crack in the specimen and we do not allow for any nucleation of the fracture as the rock strength is assigned a very large value. A discretization with

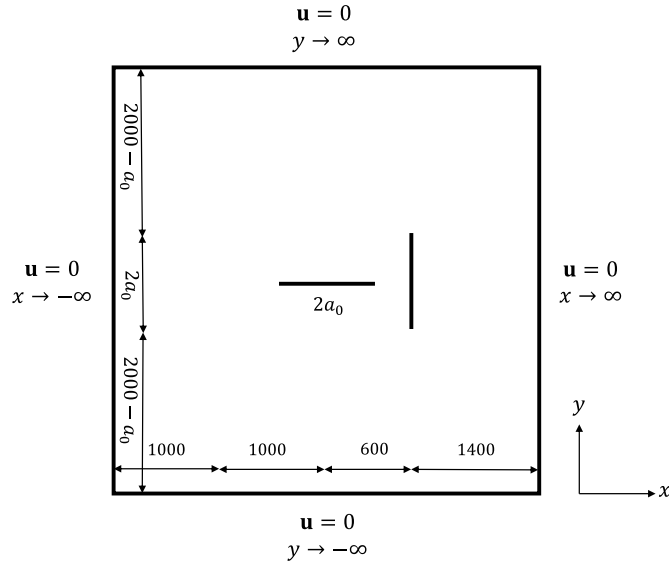


**Fig. 10.** Schematic of a square plate (unit: mm) with two pre-existing fractures. A monotonically increasing pressure with constant increments  $p = m\bar{p}$  is applied on the fracture faces.

**Table 4**

Increasing pressure leading to joining fractures: Material parameters (Wheeler et al., 2014).

Parameters	symbol	unit	value
Young's modulus	$E$	MPa	1.0
Poisson's ratio	$\nu$	—	0.2
Critical energy release rate	$g_c$	MPa·mm	1.0

28,140 standard  $P_1$  elements is applied to the problem. To capture the high gradient of pressure near the borehole, the mesh is refined in that area so that an effective mesh size of  $h \approx 0.15$  mm is adopted. The fluid is slightly compressible, and we set the fluid pressure in the borehole to 1 MPa. The other material properties are prescribed according to Table 2.

Here, the governing equation for the slightly compressible flow is written as follows (Detournay and Cheng, 1988):

$$\partial_t p + M \nabla \cdot \left( \frac{k_0}{\mu} \nabla p \right) = 0$$

where  $M = E(1 - \nu)/[(1 + \nu)(1 - 2\nu)]$  is called the constrained modulus.

Fig. 6 shows the distribution of pore pressure around the borehole for three values of dynamic viscosity  $\mu$  at early time  $t = 0.1$  s. Note that the horizontal axis is  $(r - r_0)/r_0$ , ranging from 0 to 0.25 in the direction of  $\theta = \pi/2$ . The simulation results are then compared to the analytical solution by Detournay and Cheng (Detournay and Cheng, 1988).

Fig. 7 depicts the effect of dynamic viscosity on the effective tangential stress in the vicinity of the borehole at early time  $t = 0.1$  s.

#### 4.3. Computation of the crack opening displacement

We now focus on a classical problem first solved by Sneddon and Lowengrub (1969) (see also (Bourdin et al., 2012)) that solves the opening displacement of a static line crack.

Consider a computational domain of  $\Omega = 4 \text{ m} \times 4 \text{ m}$  with a pre-existing line fracture of length  $2a_0 = 0.4 \text{ m}$ , i.e.,  $\mathcal{C} = [1.8, 2.2] \times \{0\}$ . To minimize the effect of the boundary conditions on the results, the domain size is much larger than the crack length ( $L \gg 2a_0$ ).

The mechanical properties of the material are the Young's modulus  $E = 1000 \text{ MPa}$ , the Poisson's ratio  $\nu = 0$ , and the fracture toughness  $g_c = 1 \text{ MPa's}$ .

We impose zero displacements on the external boundary of  $\Omega$ . Also we set  $d = 1$  on prescribed (initial) fracture and  $d = 0$  on the external boundary of  $\Omega$ . A monotonically increasing pressure is applied on the upper and lower faces of fracture with the magnitude  $p = 1 \text{ MPa}$ . Fig. 8 depicts the geometry and boundary conditions.

Bourdin et al. (2013) proposed a formula to compute the fracture aperture as:

$$w = \mathbf{u} \cdot \mathbf{n}_\Gamma \simeq \int_s \mathbf{u} \cdot \nabla d \, dx.$$

Then, the fracture volume is calculated by integrating the fracture aperture along the fracture's path:

$$V_f = \int_\Gamma w \, ds \simeq \int_\Omega \mathbf{u} \cdot \nabla d \, d\Omega.$$

Fig. 9 shows the aperture profile for different  $h$  and  $\ell$ . The dash line in black represents the Sneddon's analytical solution (Sneddon and Lowengrub, 1969). Also, the crack volume computed by Sneddon's analytical solution and our numerical tests are summarized in Table 3.

#### 4.4. Increasing pressure leading to joining fractures

This example motivated by Wheeler et al. (2014) demonstrates one major capability of the phase field approach that there is no need to track any complicated fracture geometry for joining fractures.

Consider a computational domain of  $\Omega = (0, 4.0) \times (0, 4.0)$  (unit: m by m) containing two pre-existing line fractures with a length of  $2a_0 = 0.4 \text{ m}$ , more precisely,  $\mathcal{C}_h = [1.8, 2.2] \times \{0\}$  and  $\mathcal{C}_v = \{2.6\} \times [1.8, 2.2]$ . To minimize the effect of the boundary conditions on the results, the domain size is much bigger than the fracture length ( $L \gg 2a_0$ ). A discretization with 19,368 standard  $P_1$  elements is applied such that an effective element size of  $h \approx 20 \text{ mm}$  is obtained in the critical zone. Also, let  $\ell = 2h$ . Fig. 10 depicts the geometric setup. A zero displacement is imposed on the boundary. Also, we set  $d = 1$  for the prescribed (initial) fractures, and  $d = 0$  on the boundary. A monotonically increasing pressure is applied on the upper and lower faces of the fracture with the magnitude  $p = m\bar{p}$  where  $\bar{p} = 0.01 \text{ MPa}$  and  $m = 1, 2, \dots, 115$ .

Following (Wheeler et al., 2014), we adopt the values of the material parameters given in Table 4.

Fig. 11 shows the phase field evolution at different load steps: (11a)  $m = 1$ , (11b)  $m = 113$ , (11c)  $m = 114$ , and (11d)  $m = 115$ . The results show that the horizontal fracture starts to propagate at  $m = 113$ , and at  $m = 114$  it intersects the vertical fracture. Overall speaking the fracture paths agree with those in (Wheeler et al., 2014). Note the fracture



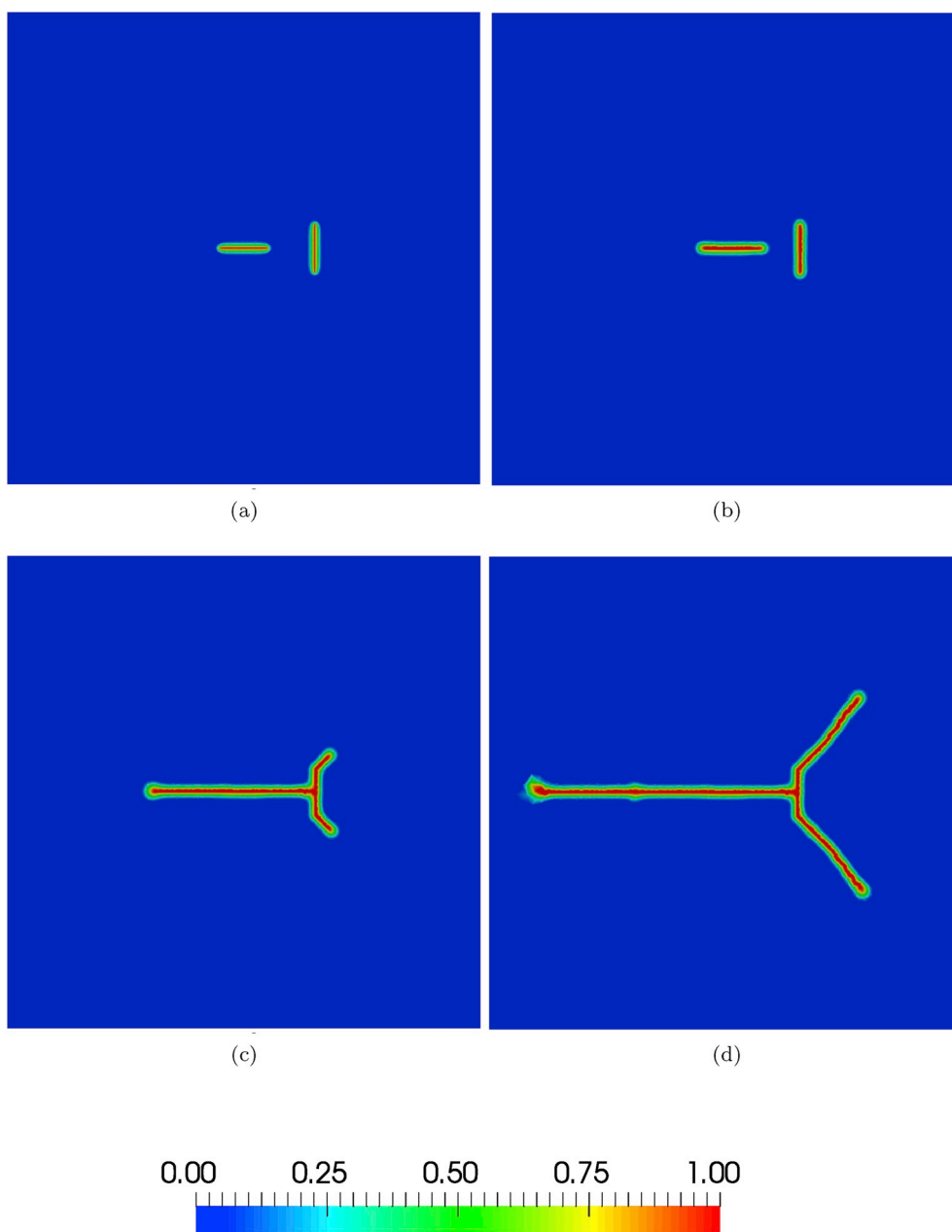


**Fig. 11.** Increasing pressure leading to joining fractures ( $p = m\bar{p}$ ). Phase field contours at different load steps (11a)  $m = 1$ , (11b)  $m = 113$ , (11c)  $m = 114$ , and (11d)  $m = 115$ . The results show that the horizontal fracture starts to propagate at  $m = 113$ , and at  $m = 114$  it intersects the vertical fracture.

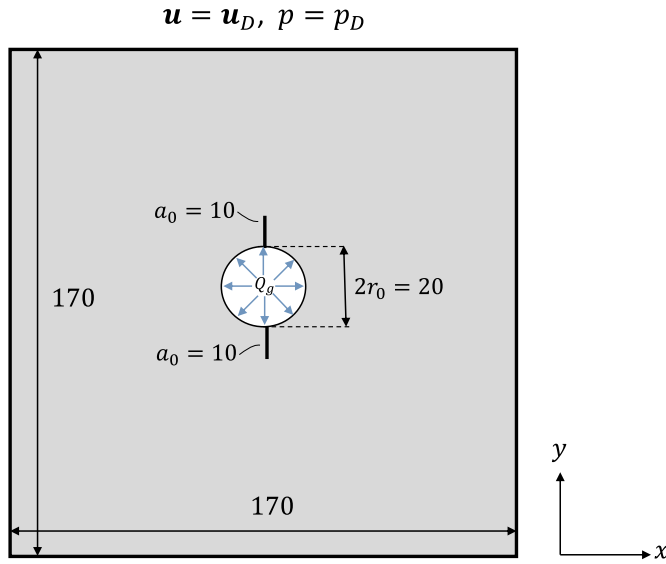


Fig. 12. Schematic of a fractured square plate (unit: mm) with pressurized CO<sub>2</sub> flow.

Table 5

Default parameter values for the examples in Sections 4.5 and 4.6. These values are taken from (Wang et al., 2018) except  $g_c$ , which is from (6).

Parameters	symbol	unit	value
Young's modulus	$E$	MPa	$6 \times 10^3$
Poisson's ratio	$\nu$	—	0.34
Critical energy release rate	$g_c$	MPa·mm	0.306
Biot coefficient	$\alpha$	—	0.85
Porosity	$\phi$	—	0.01
Initial permeability	$k_0$	mm <sup>2</sup>	$1 \times 10^{-12}$
Dynamic viscosity of CO <sub>2</sub>	$\mu$	MPa·s	$4.04 \times 10^{-11}$
Initial pressure	$p_0$	MPa	0.1
Rock's tensile strength	$\sigma_T$	MPa	11

propagation is unstable in this example.

#### 4.5. CO<sub>2</sub>-driven fracture

In this example, we investigate the fracture propagation in a square plate with a pressurized CO<sub>2</sub> flow, with (Ishida et al., 2016; Wang et al., 2018) as the benchmarks. The specimen has edge lengths of  $L = 170$  mm. The geometric setup and boundary conditions are depicted in Fig. 12. The sample is discretized into 4832 P<sub>1</sub> elements so that the mesh size  $h \approx 5.68$  mm is obtained. Also, we set  $\ell = 1.6$  mm. Table 5 shows the remaining parameters to be input.

As in Fig. 12, there exist two pre-existing fractures representing the perforations. We set  $d = 1$  for both fractures and set the Dirichlet

boundary condition  $d = 0$  on the external boundary. The fluid is continuously injected into the central borehole with diameter  $2r_0 = 20$  mm, until after the fractures propagate. Note that in this problem, the isothermal condition is adopted so that CO<sub>2</sub> is in the supercritical phase ( $T = 45$  °C).

For the sake of simplicity, the *in situ* stress  $\sigma_1 = \sigma_3 = 1$  MPa is imposed on the boundary by means of its “equivalent” prescribed displacement. More precisely, the displacement of the same specimen with no fracture under the same *in situ* stress is first computed, then used as the Dirichlet boundary condition for the problem at hand. On the external boundary, we set  $p = p_D$  where  $p_D = 0$ . Moreover,  $\Gamma_p = \Gamma_D$  in this example.

Fig. 13 shows the evolution of phase field diagram (left) and pressure profile (right) at different time steps. As seen, the fractures propagate along a straight line, and the pressure profile is accordingly distributed with the highest gradient around the borehole.

Next, we aim to calculate the breakdown pressure  $p_b$ , the pressure value when the fractures start to propagate. Fig. 14 illustrates the pressure evolution at the top of the borehole and the fracture length function. To estimate the breakdown pressure, first we output the fracture length with regard to (2). Then, we obtain the time when the slope suddenly changes in the fracture length function ( $\mathcal{G}_\ell$ ), which is the time corresponding to the breakdown pressure (here  $t \approx 0.72t_f$ ). Hence the breakdown pressure reads  $p_b = 10.9$  MPa. This value for  $p_b$  is in agreement with H-F and H-W analytical solutions. Also, our results agree with experiments results of Ishida et al. (2012) within 30%, see Table 6 and the next paragraph for more elaborations.

*Classical solutions of breakdown pressure.* There exist two classical expressions to calculate the breakdown pressure. In the case without poroelastic effect the rock deformation does not penetrate into the pressurized fracture, the Hubbert-Willis (H-W) solution applies (Hubbert and Willis, 1972):

$$p_b = 3\sigma_3 - \sigma_1 + \sigma_T,$$

in which the rock is assumed to be an elastic medium. When the porous medium is set, the Haimson-Fairhurst (H-F) solution is preferred (Haimson and Fairhurst, 1967):

$$p_b = \frac{3\sigma_3 - \sigma_1 + \sigma_T + p_0}{1 + \frac{\nu}{1-\nu}\alpha},$$

where we denote by  $p_b$  the breakdown fluid pressure,  $\sigma_3$ , and  $\sigma_1$  are the minimum and maximum principal stresses, respectively, and  $\sigma_T$  is the rock's tensile strength.

*Effect of  $N$ ,  $h$ , and  $\ell$  on the breakdown pressure.* Here we aim to study how the number of time steps  $N$ , the mesh size  $h$ , and the regularization length scale  $\ell$  affect the value of breakdown pressure. As seen in Fig. 15, the plots show similar numerical results for the pressure evolution.

*Breakdown pressure result of an anisotropic *in situ* stress.* In this example we set the maximum ( $\sigma_1 = 3$  MPa) and minimum ( $\sigma_3 = 2$  MPa) *in situ* stress. The other input data and boundary conditions are the same as aforementioned.

The pressure at the top of the borehole and the fracture length

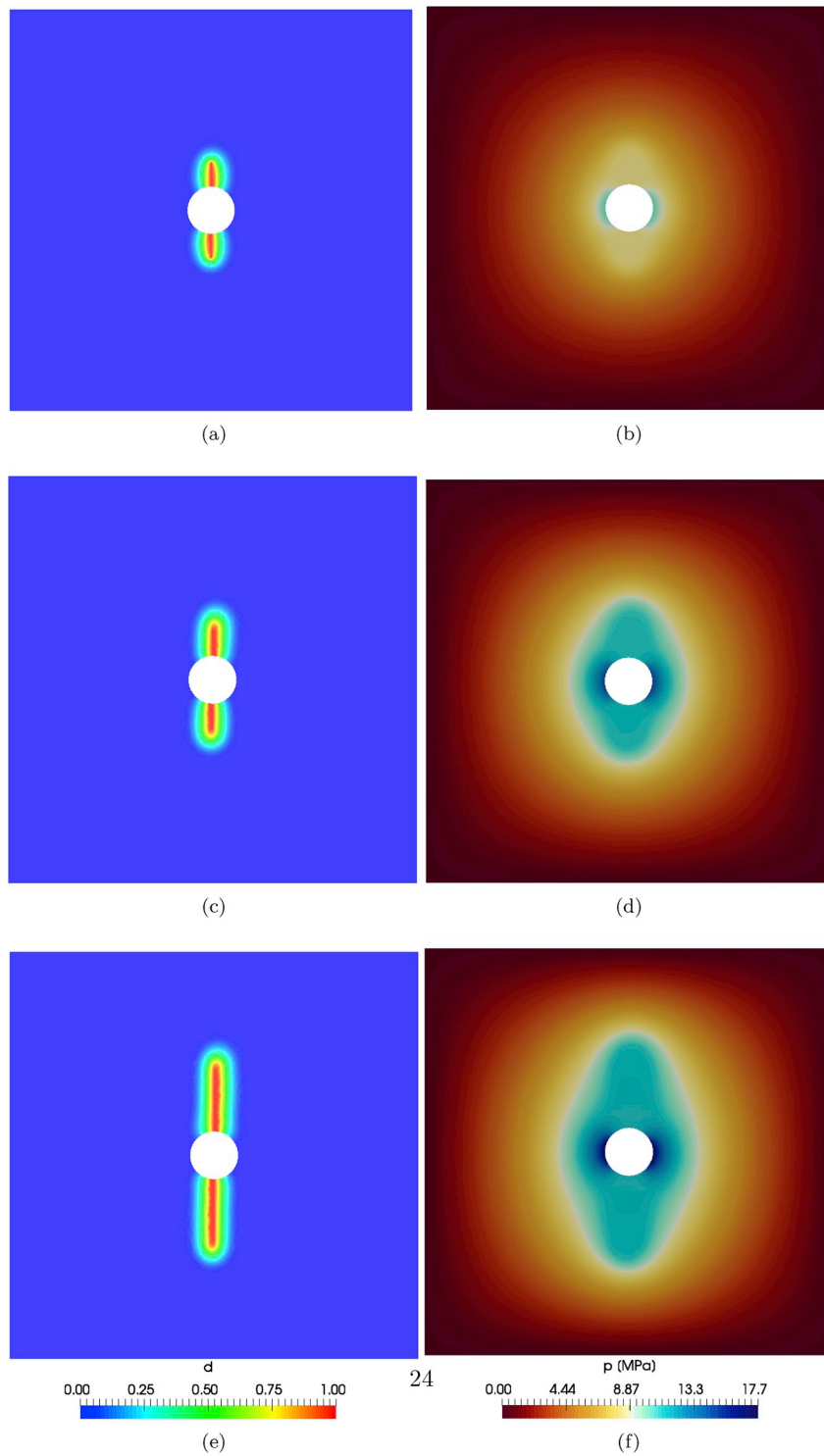


**Fig. 13.** Left: Phase field diagram at different stages (13a)  $t = 0.5t_f$ , (13c)  $t = 0.74t_f$ , and (13d)  $t = t_f$ ). Right: Pressure profile at (13b)  $t = 0.5t_f$ , (13d)  $t = 0.74t_f$ , and (13f)  $t = t_f$ .

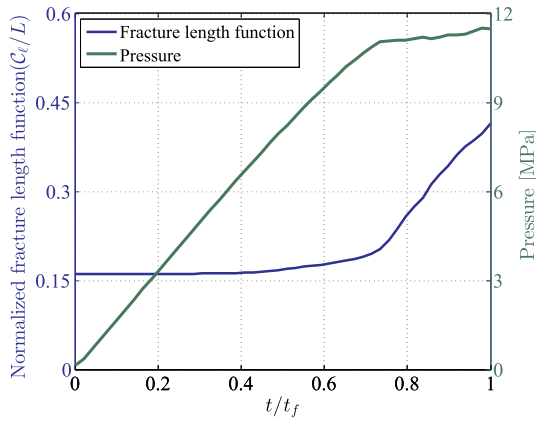


**Fig. 14.** The pressure at the top of the borehole (green line), and the fracture length function (blue line) as functions of time. The time when there is a sudden change of slope in  $\mathcal{C}_f$  assumes the time corresponding to the breakdown pressure ( $t = 0.72t_f$ ) and the corresponding breakdown pressure is  $p_b = 10.9$  MPa. This is in agreement with H-F and H-W analytical solutions.

**Table 6**

Breakdown pressure of numerical test and analytical solutions for  $\sigma_1 = \sigma_3 = 1$  MPa.

	Numerical	H-F solution	H-W solution	Experimental (Ishida et al., 2012)
$p_b$ (MPa)	10.9	11	9.1	8.44

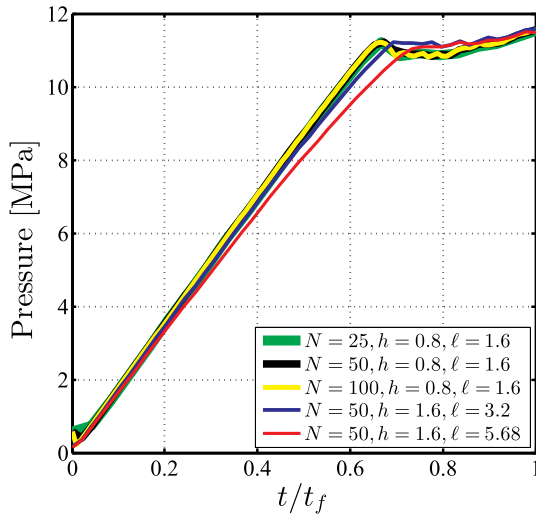


**Fig. 15.** Evolution of the pressure at the top of the borehole for different numbers of time steps  $N$ , mesh size  $h$ , and  $\ell$ .

function, (2), at different stages are illustrated in Fig. 16. The breakdown time ( $t \approx 0.77t_f$ ) and the corresponding breakdown pressure is  $p_b = 11.9$  MPa, see Table 7.

**Effect of dynamic viscosity on breakdown pressure.** We conduct several numerical examples to investigate the effect of dynamic viscosity  $\mu$  on the

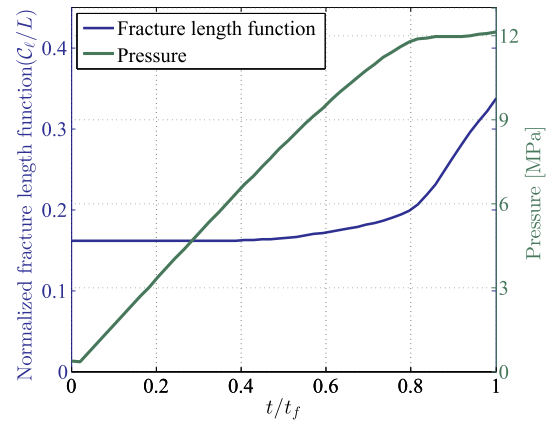


**Fig. 16.** The pressure at the top of the borehole (green line) and the fracture length function (blue line) versus time for deviatoric *in situ* stress are shown. The time ( $t \approx 0.8t_f$ ) when there is a change of slope in the fracture length function ( $\mathcal{C}_f$ ) should correspond to the breakdown pressure ( $p_b = 11.9$  MPa).

**Table 7**

Breakdown pressure of numerical test and analytical solutions for  $\sigma_1 = 3$  MPa and  $\sigma_3 = 2$  MPa.

	Numerical	H-F solution	H-W solution
$p_b$ (MPa)	11.9	14	9.8

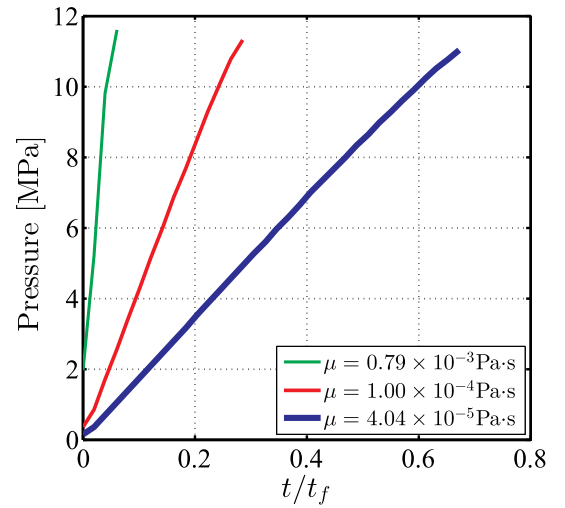


**Fig. 17.** Evolution of the pressure at the top of the borehole for different  $\mu$ 's. As seen, even though  $p_b$  is the same for different fracturing fluids, by increasing  $\mu$ , the breakdown pressure is reached earlier.

breakdown pressure  $p_b$ . In this set of examples an effective mesh size, the mesh size near the borehole or the fractures,  $h \approx 1.6$  mm is adopted. Also, we set  $\ell = 2h$ . In Fig. 17 we plot the pressure evolution up to the time when  $\mathcal{C}_f(t)$  changes slope, so that the end points correspond to the breakdown pressures. The results indicate that  $p_b$  is approximately the

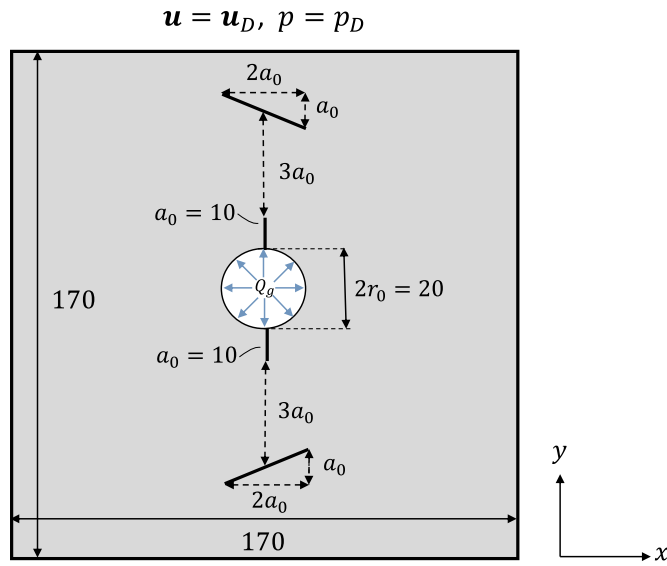


**Fig. 18.** Interaction between CO<sub>2</sub>-driven fracture and inclined natural fractures. The geometric setup and boundary conditions are shown (unit: mm). There exist two CO<sub>2</sub>-driven fractures and two inclined natural ones.

same for different fluid viscosities, but the time when the breakdown pressure is reached differs. Fig. 17 demonstrates that the rock will break earlier for the fluid with bigger dynamic viscosity. Also it shows that regardless of the fracturing fluid, the breakdown pressure is slightly the same for all cases. This is in accordance with the physics that the breakdown pressure normally reflects the strength of the solid. However, Wang et al. (2018) reported different breakdown pressures for different fluids which also agrees with some experiments (Ishida et al., 2012, 2016). We believe this discrepancy demands further research.

#### 4.6. Interaction between CO<sub>2</sub>-driven fractures and natural fractures

In this example, we investigate the interaction between two CO<sub>2</sub>-driven fractures and two inclined natural fractures. The specimen has edge lengths of  $L = 170$  mm. The geometric setup and boundary conditions are depicted in Fig. 18. The sample is discretized into 32,736 P<sub>1</sub> elements so that the mesh size  $h \approx 6.25 \times 10^{-1}$  mm is obtained. Also, we set  $\ell = 4h$ . The remaining input data can be found in Table 5.

As in Fig. 18, there exist two pre-existing vertical fractures representing the perforations and two inclined natural fractures. We set  $d = 1$  for both initial and inclined natural fractures, and the Dirichlet boundary condition  $d = 0$  is imposed on the external boundaries. The fluid is continuously injected into the central borehole with diameter  $2r_0 = 20$  mm. The *in situ* stress with the value of  $\sigma_1 = \sigma_3 = 1$  MPa is also imposed on the boundary by means of its 'equivalent' prescribed displacement. See Section 4.5 for more descriptions.

Fig. 19 shows the evolution of the phase field profile (left) and the pressure profile (right) at different time steps. As seen, the vertical fractures propagate along a straight line until  $t = 0.4t_f$ . Then, near the inclined natural fractures, the CO<sub>2</sub>-driven fractures turn to join them with an angle of approximately 90° at  $t = 0.8t_f$ . In the last frame, Fig. 19g, the vertical fractures deviate into the inclined natural fractures and propagate from left tips. This fracture evolving pattern is called 'crossing with an offset' which is one possible interaction process of hydraulic fracture and natural fracture (Yew and Weng, 2014).

#### 5. Conclusions

We have proposed and verified a phase field approach to simulate CO<sub>2</sub> fracturing, with CO<sub>2</sub> treated as a compressible fluid. In one of the numerical examples, the breakdown pressure agrees well with widely

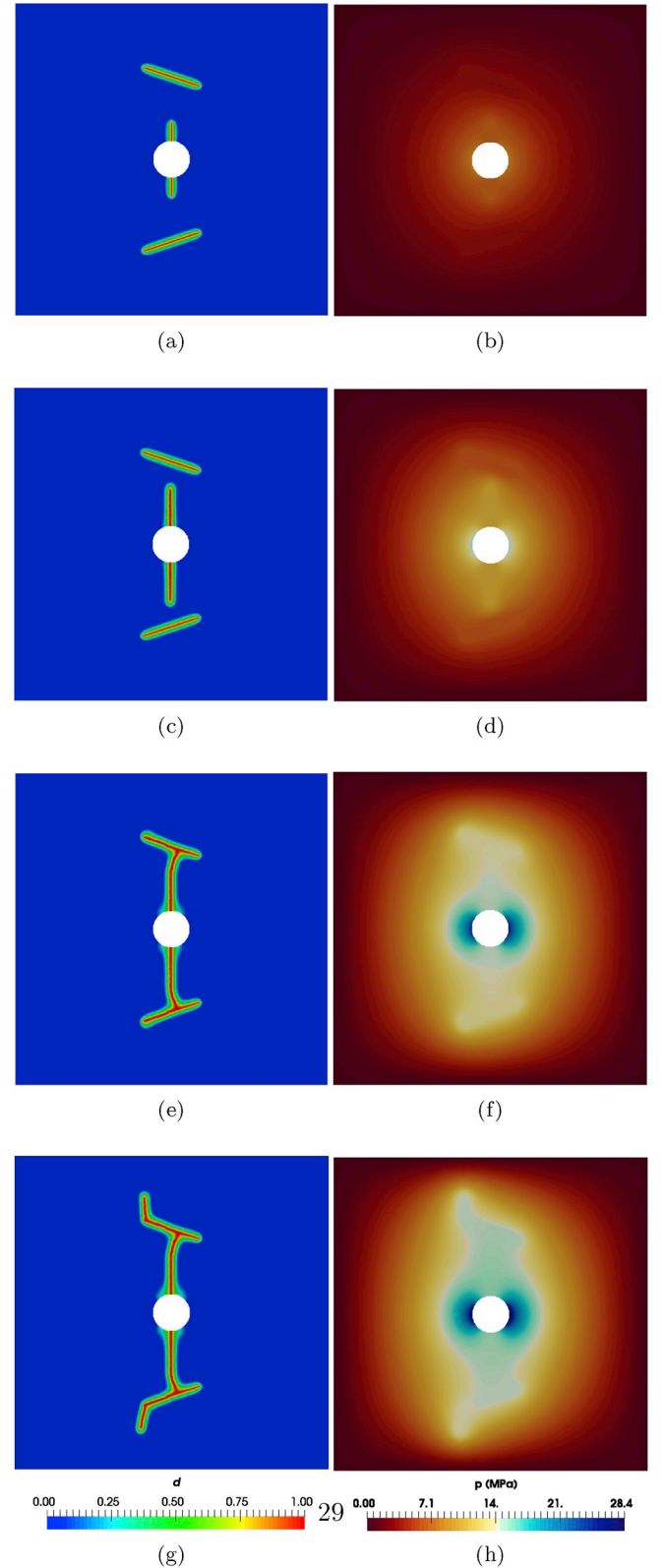


**Fig. 19.** Left: Phase field diagram at different stages (19a)  $t = 0.$ , (19c)  $t = 0.4t_f$ , (19e)  $t = 0.8t_f$ , and (19g)  $t = t_f$ . Right: Pressure profile at (19b)  $t = 0.$ , (19d)  $t = 0.4t_f$ , (19f)  $t = 0.8t_f$ , and (19h)  $t = t_f$ . As seen, the vertical fractures propagate along a straight line until they reached the natural fractures. Then, they deviate into the inclined natural fractures, and continue evolving from left tips. 'Crossing with an offset' is one possible interaction process of hydraulic fracture and natural fracture (Yew and Weng, 2014).



used analytical solutions. Also, the results agree with experimental results within 30%. While this work represents the first of its kind, potentially the phase field approach allows complicated modeling of fracture initiation and branching.

## Acknowledgments

This work is supported by the National Natural Science Foundation of China with grant #11402146. YS also acknowledges the financial support by the Young 1000 Talent Program of China.

## Appendix A. Weak forms and discretized formulations

Here we provide weak forms useful for FEniCS implementation. For more information on implementing the phase field approach for fracture, see (Shen et al., 2018).

### Appendix A.1. Porous medium

To proceed, let the test function spaces be

$$\mathcal{V}_{\bar{\mathbf{u}}} := \{\bar{\mathbf{u}} \in H^1(\Omega; \mathbb{R}^2) | \bar{\mathbf{u}} = 0 \text{ on } \Gamma_D\},$$

$$\mathcal{V}_{\bar{d}} := H^1(\Omega).$$

Then we derive the first variations of the energy functional (3), which will be needed for stating the weak form:

$$\begin{aligned} \delta \Pi_\ell[(\mathbf{u}, d); \bar{\mathbf{u}}] &= \int_{\Omega} \boldsymbol{\sigma}[\boldsymbol{\varepsilon}(\mathbf{u}), d] : \boldsymbol{\varepsilon}(\bar{\mathbf{u}}) d\Omega - \int_{\Gamma_N} \mathbf{t}_N \cdot \bar{\mathbf{u}} d\Gamma - \int_{\Omega} \mathbf{b} \cdot \bar{\mathbf{u}} d\Omega \\ &+ \int_{\Omega} (\alpha - 1) \nabla((1 - d)^2 p) \cdot \bar{\mathbf{u}} d\Omega + \int_{\Omega} (1 - d)^2 \nabla p \cdot \bar{\mathbf{u}} d\Omega \end{aligned} \quad (\text{A.1a})$$

$$\begin{aligned} \delta \Pi_\ell[(\mathbf{u}, d); \bar{d}] &= \int_{\Omega} (\alpha - 1) g'(d) \bar{d} p \operatorname{div} \mathbf{u} d\Omega + \int_{\Omega} g'(d) \bar{d} \nabla p \cdot \mathbf{u} d\Omega \\ &+ \int_{\Omega} g'(d) \psi_+(\varepsilon) \bar{d} d\Omega + \frac{g_c}{4c_w} \int_{\Omega} \left( \frac{\omega'(d) \bar{d}}{\ell} + 2\ell \nabla d \cdot \nabla \bar{d} \right) d\Omega. \end{aligned} \quad (\text{A.1b})$$

The weak form can thus be stated as: Find  $(\mathbf{u} \times d) \in \mathcal{S}_{\mathbf{u}} \times \mathcal{S}_d$ , such that for all admissible functions  $(\bar{\mathbf{u}} \times \bar{d}) \in \mathcal{V}_{\mathbf{u}} \times \mathcal{V}_d$ ,  $\delta \Pi_\ell[(\mathbf{u}, d); \bar{\mathbf{u}}] = 0$  and  $\delta \Pi_\ell[(\mathbf{u}, d); \bar{d}] = 0$ .

Also we take another variation from (3) which will be needed for the discretized formulation:

$$\delta^2 \Pi_\ell[(\mathbf{u}, d); \bar{\mathbf{u}}, \delta \mathbf{u}] = \int_{\Omega} \boldsymbol{\varepsilon}(\delta \mathbf{u}) : \mathbb{C}[\boldsymbol{\varepsilon}(\mathbf{u}), d] : \boldsymbol{\varepsilon}(\bar{\mathbf{u}}) d\Omega, \quad (\text{A.2a})$$

$$\begin{aligned} \delta^2 \Pi_\ell[(\mathbf{u}, d); \bar{d}, \delta d] &= \int_{\Omega} \delta d g''(d) \psi_+(\varepsilon) \bar{d} d\Omega \\ &+ \int_{\Omega} (\alpha - 1) g''(d) \bar{d} \delta d p \operatorname{div} \mathbf{u} d\Omega + \int_{\Omega} g''(d) \bar{d} \delta d \nabla p \cdot \mathbf{u} d\Omega \\ &+ \frac{g_c}{4c_w} \int_{\Omega} \left[ \frac{\delta d w''(d) \bar{d}}{\ell} + 2\ell \nabla(\delta d) \cdot \nabla \bar{d} \right] d\Omega, \end{aligned} \quad (\text{A.2b})$$

where the fourth-order tensor  $\mathbb{C}[\boldsymbol{\varepsilon}(\mathbf{u}), d] = \frac{\partial \boldsymbol{\sigma}(\boldsymbol{\varepsilon}, d)}{\partial \boldsymbol{\varepsilon}}|_{\boldsymbol{\varepsilon}=\boldsymbol{\varepsilon}(\mathbf{u})}$  is the tangent elasticity tensor.

To discretize the problem, we divide  $\Omega$  with a conforming mesh  $\mathcal{T}_h$  of triangular elements. Let  $\eta$  be the set of nodes of  $\mathcal{T}_h$ . We approximate  $(\mathbf{u}, d)$  with the standard  $P_1$  finite element basis functions associated with all nodes  $i \in \eta$ :

$$\mathbf{u}(\mathbf{x}) = \sum_{i \in \eta} \mathbf{N}_i^u(\mathbf{x}) \mathbf{u}_i, \quad d(\mathbf{x}) = \sum_{i \in \eta} N_i(\mathbf{x}) d_i, \quad (\text{A.3})$$

where  $\mathbf{u}_i$ , and  $d_i$  are the displacement and phase field values at node  $i$ , respectively; and  $\mathbf{N}_i^u$  is given by:

$$\mathbf{N}_i^u = \begin{bmatrix} N_i & 0 \\ 0 & N_i \end{bmatrix},$$

where  $N_i$  is the standard finite element shape function associated with  $i \in \eta$ , satisfying  $N_j(\mathbf{x}_i) = \delta_{ji}$ , for all  $i, j \in \eta$ , and  $\mathbf{x}_i, \mathbf{u}_i \in \mathbb{R}^2$  are the position vector and nodal displacement vector of node  $i$ , respectively. Note that we also apply the same discretization to the test functions.

**Discretized weak form.** Let  $n_{\text{nodes}}$  denote the number of nodes in  $\eta$ . Let  $\mathbf{u} \in \mathbb{R}^{2n_{\text{nodes}}}$ ,  $\mathbf{d} \in \mathbb{R}^{n_{\text{nodes}}}$  contain all entries of  $\mathbf{u}_i, d_i$ , respectively, for all  $i \in \eta$ . The discretized residuals can be written as  $\mathbb{U}_i(\mathbf{u}) := \delta \Pi(\mathbf{u}; \mathbf{N}_i^u) \in \mathbb{R}^2$  and  $\mathbb{D}_i(d) := \delta \Pi(d; N_i) \in \mathbb{R}$  for all  $i \in \eta$ . With (A.1), these residual vectors are expressed as follows:

$$\begin{aligned} \mathbb{U}_i &= \int_{\Omega} (\mathbf{B}_i)^T \boldsymbol{\sigma}[\boldsymbol{\varepsilon}(\mathbf{u}), d] d\Omega - \int_{\Gamma_N} (\mathbf{N}_i^u)^T \mathbf{t}_N d\Gamma - \int_{\Omega} (\mathbf{N}_i^u)^T \mathbf{b} d\Omega \\ &+ \int_{\Omega} (\alpha - 1) (\mathbf{N}_i^u)^T \nabla((1 - d)^2 p) d\Omega + \int_{\Omega} (\mathbf{N}_i^u)^T (1 - d)^2 \nabla p d\Omega \\ \mathbb{D}_i &= \int_{\Omega} (\alpha - 1) g'(d) N_i p \operatorname{div} \mathbf{u} d\Omega + \int_{\Omega} g'(d) N_i (\nabla p)^T \mathbf{u} d\Omega \\ &+ \int_{\Omega} g'(d) \psi_+(\varepsilon) N_i d\Omega + \frac{g_c}{4c_w} \int_{\Omega} \left( \frac{w'(d) N_i}{\ell} + 2\ell \nabla d \cdot \nabla N_i \right) d\Omega, \end{aligned} \quad (\text{A.4})$$

where  $\mathbb{U}_i$  is also called the nodal force at  $i$ . Also note that in (A.4),  $\boldsymbol{\sigma}$  is understood as a 3-vector, and the strain-displacement matrix for node  $i$  are given by:

$$\mathbf{B}_i = \begin{bmatrix} N_{i,x} & 0 \\ 0 & N_{i,y} \\ N_{i,y} & N_{i,x} \end{bmatrix}.$$

The discretized weak form is  $\mathbb{U}_i = 0$  for all nodes  $i$  at which  $\mathbf{u}$  is not prescribed, and  $\mathbb{D}_i = 0$  for all nodes  $i$  at which  $d$  is not prescribed.

**Tangent stiffness matrices.** The tangent stiffness matrices are needed for Newton-Raphson algorithms. The tangent stiffness matrix components of (A.2) are  $\mathbf{K}_{ij}^u := \partial \mathbb{U}_i / \partial \mathbf{u}_j = \delta^2 \Pi[\mathbf{u}; \mathbf{N}_i^u, \mathbf{N}_j^u] \in \mathbb{R}^{2 \times 2}$  for all  $i, j \in \eta$  and  $K_{ij}^d := \partial \mathbb{D}_i / \partial d_j = \delta^2 \Pi[d; N_i, N_j] \in \mathbb{R}$  for all  $i, j \in \eta$ , which can be expressed as follows:

$$\mathbf{K}_{ij}^u = \int_{\Omega} (\mathbf{B}_i)^T \mathbf{D} \mathbf{B}_j d\Omega, \quad (\text{A.5a})$$

$$\begin{aligned} K_{ij}^d &= \int_{\Omega} (\alpha - 1) g''(d) N_i N_j p \operatorname{div} \mathbf{u} d\Omega + \int_{\Omega} g''(d) N_i N_j (\nabla p)^T \mathbf{u} d\Omega \\ &+ \int_{\Omega} g''(d) \psi_+(\varepsilon) N_i N_j d\Omega + \frac{g_c}{4c_w} \int_{\Omega} \left[ \frac{w''(d) N_i N_j}{\ell} + 2\ell (\nabla N_i)^T \nabla N_j \right] d\Omega, \end{aligned} \quad (\text{A.5b})$$

where we denote by  $\mathbf{D}$  the matrix form of the tangent elastic modulus tensor  $\mathbb{C}$ . Below we give its expression  $\mathbf{D} = g(d)\mathbf{D}_+ + \mathbf{D}_-$  for our adopted tension-compression decomposition (Amor et al., 2009):

$$\mathbf{D}_+ = BH(\operatorname{tr} \varepsilon) \begin{bmatrix} 1 & 1 & 0 \\ 1 & 1 & 0 \\ 0 & 0 & 0 \end{bmatrix} + \frac{G}{3} \begin{bmatrix} 4 & -2 & 0 \\ -2 & 4 & 0 \\ 0 & 0 & 3 \end{bmatrix},$$

$$\mathbf{D}_- = BH(-\operatorname{tr} \varepsilon) \begin{bmatrix} 1 & 1 & 0 \\ 1 & 1 & 0 \\ 0 & 0 & 0 \end{bmatrix},$$

where  $B = E/[3(1 - 2\nu)]$  is the bulk modulus. Here,  $H$  is the Heaviside function such that  $H(a) = 1$  if  $a > 0$ ,  $H(a) = 0$  if  $a < 0$ , and  $H(a) = \frac{1}{2}$  if  $a = 0$ .

#### Appendix A.2. Compressible ( $\text{CO}_2$ ) fluid flow discretization

The compressible fluid flow discretization is also done via the finite element method. We first discretize in time and then in space. We will adopt the backward Euler method for time discretization.

To proceed, let the admissible set of pressure be:

$$\mathcal{S}_p := \{p \in H^1(\Omega) \mid p = p_D \text{ on } \Gamma_p\}.$$

The test function space can be defined as:

$$\mathcal{V}_p := \{\bar{p} \in H^1(\Omega) \mid \bar{p} = 0 \text{ on } \Gamma_p\}.$$

The weak form can be stated as: find  $p \in \mathcal{S}_p$  such that for all admissible functions  $\bar{p} \in \mathcal{V}_p$ ,

$$\begin{aligned} &\frac{1}{\Delta t} \int_{\Omega} \phi(\rho - \rho^{n-1}) \bar{p} d\Omega + \frac{1}{\Delta t} \int_{\Omega} \rho(\varepsilon_v - \varepsilon_v^{n-1}) \bar{p} d\Omega \\ &+ \int_{\Omega} \rho \frac{k(d)}{\mu} \nabla p \cdot \nabla \bar{p} d\Omega - \int_{\Gamma_B} Q_g \bar{p} d\Gamma = 0, \end{aligned} \quad (\text{A.6})$$

where  $\rho^{n-1}$  and  $\varepsilon_v^{n-1}$  denote solutions at the previous time step.

Also, we use the conventional finite element shape functions  $\{N_i\}$  for  $p$ :

$$p(\mathbf{x}) = \sum_{i \in \eta} p_i N_i(\mathbf{x}). \quad (\text{A.7})$$

Thus, the residual vector form of A.6 is expressed as follows:

$$\begin{aligned} \mathbb{P}_i &:= \frac{1}{\Delta t} \int_{\Omega} \phi(\rho - \rho^{n-1}) N_i d\Omega + \frac{1}{\Delta t} \int_{\Omega} \rho(\varepsilon_v - \varepsilon_v^{n-1}) N_i d\Omega \\ &+ \int_{\Omega} \rho \frac{k(d)}{\mu} (\nabla p)^T \nabla N_i d\Omega - \int_{\Gamma_B} Q_g N_i d\Gamma. \end{aligned} \quad (\text{A.8})$$

The discretized weak form is  $\mathbb{P}_i = 0$  for all nodes  $i$  at which  $p$  is not prescribed.

The tangent stiffness matrix form of the fluid flow  $K_{ij}^p := \partial \mathbb{P}_i / \partial p_j$  for all  $i, j \in \eta$ , which can be expressed as follows:

$$K_{ij}^p := \int_{\Omega} \rho \frac{k(d)}{\mu} (\nabla N_i)^T \nabla N_j d\Omega. \quad (\text{A.9})$$

#### Appendix B. Supplementary data

Supplementary data to this article can be found online at <https://doi.org/10.1016/j.jngse.2019.102905>.

## References

- Ambati, M., Gerasimov, T., De Lorenzis, L., 2015. A review on phase-field models of brittle fracture and a new fast hybrid formulation. *Comput. Mech.* 55 (2), 383–405.
- Ambrosio, L., Tortorelli, V.M., 1990. On the Approximation of Free Discontinuity Problems. *Scuola Normale Superiore*.
- Ambrosio, L., Tortorelli, V.M., 1992. On the approximation of functionals depending on jumps by quadratic, elliptic functionals. *Boll. Unione Mat. Ital.* 6, 105–123.
- Amestoy, P.R., Duff, I.S., L'Excellent, J.-Y., Koster, J., 2000. MUMPS: a general purpose distributed memory sparse solver. In: *International Workshop on Applied Parallel Computing*. Springer, pp. 121–130.
- Amor, H., Marigo, J.-J., Maurini, C., 2009. Regularized formulation of the variational brittle fracture with unilateral contact: numerical experiments. *J. Mech. Phys. Solids* 57, 1209–1229.
- Balay, S., Abhyankar, S., Adams, M.F., Brown, J., Brune, P., Buschelman, K., Dalcin, L., Eijkhout, V., Gropp, W.D., Kaushik, D., Knepley, M.G., May, D.A., McInnes, L.C., Mills, R.T., Munson, T., Rupp, K., Sanan, P., Smith, B.F., Zampini, S., Zhang, H., Zhang, H., 2018. PETSc Users Manual, Tech. Rep. ANL-95/11 - Revision 3.9. Argonne National Laboratory.
- Bilgen, C., Kopaničáková, A., Krause, R., Weinberg, K., 2018. A phase-field approach to conchoidal fracture. *Meccanica* 53 (6), 1203–1219.
- Bourdin, B., Francfort, G.A., Marigo, J.-J., 2000. Numerical experiments in revisited brittle fracture. *J. Mech. Phys. Solids* 48 (4), 797–826.
- Bourdin, B., Francfort, G.A., Marigo, J.J., 2008. The variational approach to fracture. *J. Elast.* 91, 5–148.
- Bourdin, B., Chukwudozie, C.P., Yoshioka, K., 2012. A variational approach to the numerical simulation of hydraulic fracturing. In: *SPE Annual Technical Conference and Exhibition*. Society of Petroleum Engineers SPE-159154-MS.
- Bourdin, B., Chukwudozie, C., Yoshioka, K., 2013. A variational approach to the numerical simulation of hydraulic fracturing. In: *Jirásek, M., Allix, O., Moës, N., Oliver, J. (Eds.), Computational Modeling of Fracture and Failure of Materials and Structures: Proceedings of CFRAC 2013*, pp. 180.
- Bourdin, B., Marigo, J.-J., Maurini, C., Sicsic, P., 2014. Morphogenesis and propagation of complex cracks induced by thermal shocks. *Phys. Rev. Lett.* 112, 014301.
- Brown, D.W., 2000. A hot dry rock geothermal energy concept utilizing supercritical CO<sub>2</sub> instead of water. In: *Proceedings of the Twenty-Fifth Workshop on Geothermal Reservoir Engineering*. Stanford University, pp. 233–238.
- Chukwudozie, C., 2016. Application of the Variational Fracture Model to Hydraulic Fracturing in Poroelastic Media. Ph.D. thesis. Louisiana State University.
- Civan, F., 2010. Effective correlation of apparent gas permeability in tight porous media. *Transport Porous Media* 82 (2), 375–384.
- Culp, D., Tupek, M.R., Newell, P., Hubler, M.H., 2017. Phase-field modeling of fracture in CO<sub>2</sub> sequestration. In: *51st US Rock Mechanics/Geomechanics Symposium*. American Rock Mechanics Association ARMA-2017-0644.
- Detournay, E., Cheng, A.-D., 1988. Poroelastic response of a borehole in a non-hydrostatic stress field. In: *International Journal of Rock Mechanics and Mining Sciences & Geomechanics Abstracts*, vol. 25. Elsevier, pp. 171–182.
- Detournay, E., Garagash, D., 2003. The near-tip region of a fluid-driven fracture propagating in a permeable elastic solid. *J. Fluid Mech.* 494, 1–32.
- Ehlers, W., Luo, C., 2017. A phase-field approach embedded in the theory of porous media for the description of dynamic hydraulic fracturing. *Comput. Methods Appl. Mech. Eng.* 315, 348–368.
- Francfort, G.A., Marigo, J.-J., 1998. Revisiting brittle fracture as an energy minimization problem. *J. Mech. Phys. Solids* 46 (8), 1319–1342.
- Haimson, B., Fairhurst, C., 1967. Initiation and extension of hydraulic fractures in rocks. *Soc. Petrol. Eng. J.* 7 (03), 310–318.
- Hattori, G., Trevelyan, J., Augarde, C.E., Coombs, W.M., Aplin, A.C., 2017. Numerical simulation of fracking in shale rocks: current state and future approaches. *Arch. Comput. Methods Eng.* 24 (2), 281–317.
- Heider, Y., Markert, B., 2017. Modelling of hydraulic fracturing and fluid flow change in saturated porous domains. *Proc. Appl. Math. Mech.* 17 (1), 95–98.
- Hosseini, S.A., Javadpour, F., Michael, G.E., 2015. Novel analytical core-sample analysis indicates higher gas content in shale-gas reservoirs. *SPE J.* 20 (6), 1–397.
- Hu, J., Garagash, D., 2010. Plane-strain propagation of a fluid-driven crack in a permeable rock with fracture toughness. *J. Eng. Mech.* 136 (9), 1152–1166.
- Hubbert, M.K., Willis, D.G., 1972. *Mechanics of Hydraulic Fracturing*. AAPG Special Volumes.
- Ishida, T., Aoyagi, K., Niwa, T., Chen, Y., Murata, S., Chen, Q., Nakayama, Y., 2012. Acoustic emission monitoring of hydraulic fracturing laboratory experiment with supercritical and liquid CO<sub>2</sub>. *Geophys. Res. Lett.* 39 (16), L16309.
- Ishida, T., Chen, Y., Bennour, Z., Yamashita, H., Inui, S., Nagaya, Y., Naoi, M., Chen, Q., Nakayama, Y., Nagano, Y., 2016. Features of CO<sub>2</sub> fracturing deduced from acoustic emission and microscopy in laboratory experiments. *J. Geophys. Res. Solid Earth* 121 (11), 8080–8098.
- Javadpour, F., 2009. Nanopores and apparent permeability of gas flow in mudrocks (shales and siltstone). *J. Can. Pet. Technol.* 48 (8), 16–21.
- Javadpour, F., Fisher, D., Unsworth, M., 2007. Nanoscale gas flow in shale gas sediments. *J. Can. Pet. Technol.* 46 (10).
- Lillies, A.T., King, S.R., 1982. Sand fracturing with liquid carbon dioxide. In: *SPE Production Technology Symposium*. Society of Petroleum Engineers SPE-11341-MS.
- Logg, A., Wells, G.N., Hake, J., 2012. DOLFIN: A C++/Python Finite Element Library. Springer Berlin Heidelberg, Berlin, Heidelberg.
- Lu, Y.L., Elsworth, D., Wang, L.G., 2013. Microcrack-based coupled damage and flow modeling of fracturing evolution in permeable brittle rocks. *Comput. Geotech.* 49, 226–244.
- Mauthe, S., Miehe, C., 2017. Hydraulic fracture in poro-hydro-elastic media. *Mech. Res. Commun.* 80, 69–83.
- Middleton, R., Viswanathan, H., Currier, R., Gupta, R., 2014. CO<sub>2</sub> as a fracturing fluid: potential for commercial-scale shale gas production and CO<sub>2</sub> sequestration. *Energy Procedia* 63, 7780–7784.
- Middleton, R.S., Carey, J.W., Currier, R.P., Hyman, J.D., Kang, Q., Karra, S., Jiménez-Martínez, J., Porter, M.L., Viswanathan, H.S., 2015. Shale gas and non-aqueous fracturing fluids: opportunities and challenges for supercritical CO<sub>2</sub>. *Appl. Energy* 147, 500–509.
- Miehe, C., Hofacker, M., Welschinger, F., 2010a. A phase field model for rate-independent crack propagation: robust algorithmic implementation based on operator splits. *Comput. Methods Appl. Mech. Eng.* 199 (45–48), 2765–2778.
- Miehe, C., Hofacker, M., Welschinger, F., 2010b. A phase field model for rate-independent crack propagation: robust algorithmic implementation based on operator splits. *Comput. Methods Appl. Mech. Eng.* 199 (45–48), 2765–2778.
- Miehe, C., Welschinger, F., Hofacker, M., 2010c. Thermodynamically consistent phase-field models of fracture: variational principles and multi-field FE implementations. *Int. J. Numer. Methods Eng.* 83 (10), 1273–1311.
- Mikelic, A., Wheeler, M.F., 2013. Convergence of iterative coupling for coupled flow and geomechanics. *Comput. Geosci.* 17 (3), 455–461.
- Mikelic, A., Wheeler, M.F., Wick, T., 2014. Phase-Field Modeling of Pressurized Fractures in a Poroelastic Medium. ICES Report, pp. 14–18.
- Miller, J., Johansen, R.T., 1976. Fracturing Oil Shale with Explosives for in Situ Recovery, Shale Oil, Tar Sands, and Related Fuel Sources. pp. 98–111.
- Moës, N., Dolbow, J., Belytschko, T., 1999. A finite element method for crack growth without remeshing. *Int. J. Numer. Methods Eng.* 46 (1), 131–150.
- Munson, T., Sarich, J., Wild, S., Benson, S., McInnes, L., 2014. Toolkit for Advanced Optimization (TAO) Users Manual. Tech. rep., Technical Report No. ANL/MCS-TM-322-Revision 3.5. Argonne National Laboratory 2014.
- Ngo, D., Scordelis, A.C., 1967. Finite element analysis of reinforced concrete beams. *Int. Concr. Abstr.* 64 (3), 152–163.
- Peerlings, R.H.J., de Borst, R., Brekelmans, W.A.M., de Vree, J.H.P., 1996. Gradient enhanced damage for quasi-brittle materials. *Int. J. Numer. Methods Eng.* 39 (19), 3391–3403.
- Pillai, U., Heider, Y., Markert, B., 2018. A diffusive dynamic brittle fracture model for heterogeneous solids and porous materials with implementation using a user-element subroutine. *Comput. Mater. Sci.* 153, 36–47.
- Rangarajan, R., Chiaramonte, M.M., Hunsweck, M.J., Shen, Y., Lew, A.J., 2015. Simulating curvilinear crack propagation in two dimensions with universal meshes. *Int. J. Numer. Methods Eng.* 102 (3–4), 632–670.
- Shen, Y., Mollaali, M., Li, Y., Ma, W., Jiang, J., 2018. Implementation details for the phase field approaches to fracture. *J. Shanghai Jiaotong Univ. (Sci.)* 23 (1), 166–174.
- Sneddon, I.N., Lowengrub, M., 1969. *Crack Problems in the Classical Theory of Elasticity*. Wiley, New York.
- Span, R., Wagner, W., 1996. A new equation of state for carbon dioxide covering the fluid region from the triple-point temperature to 1100 K at pressures up to 800 MPa. *J. Phys. Chem. Ref. Data* 25 (6), 1509–1596.
- Suehiro, Y., Nakajima, M., Yamada, K., Uematsu, M., 1996. Critical parameters of {xCO<sub>2</sub> + (1-x) CHF<sub>3</sub>} for x = (1.0000, 0.7496, 0.5013, and 0.2522). *J. Chem. Thermodyn.* 28 (10), 1153–1164.
- Tanné, E., Li, T., Bourdin, B., Marigo, J.-J., Maurini, C., 2018. Crack nucleation in variational phase-field models of brittle fracture. *J. Mech. Phys. Solids* 110, 80–99.
- Verhoosel, C.V., Scott, M.A., Hughes, T.J., De Borst, R., 2011. An isogeometric analysis approach to gradient damage models. *Int. J. Numer. Methods Eng.* 86 (1), 115–134.
- Wang, L., Yao, B., Cha, M., Alqahtani, N.B., Patterson, T.W., Kneafsey, T.J., Miskimins, J.L., Yin, X., Wu, Y.-S., 2016. Waterless fracturing technologies for unconventional reservoirs—opportunities for liquid nitrogen. *J. Nat. Gas Sci. Eng.* 35, 160–174.
- Wang, J., Elsworth, D., Wu, Y., Liu, J., Zhu, W., Liu, Y., 2018. The influence of fracturing fluids on fracturing processes: a comparison between water, oil and SC-CO<sub>2</sub>. *Rock Mech. Rock Eng.* 51 (1), 299–313.
- Wheeler, M.F., Wick, T., Wollner, W., 2014. An augmented-Lagrangian method for the phase-field approach for pressurized fractures. *Comput. Methods Appl. Mech. Eng.* 271, 69–85.
- Wick, T., Singh, G., Wheeler, M.F., 2016. Fluid-filled fracture propagation with a phase-field approach and coupling to a reservoir simulator. *SPE J.* 21 (03), 981–999.
- Wilson, Z.A., Landis, C.M., 2016. Phase-field modeling of hydraulic fracture. *J. Mech. Phys. Solids* 96, 264–290.
- Yew, C.H., Weng, X., 2014. *Mechanics of Hydraulic Fracturing*. Gulf Professional Publishing.
- Yoshioka, K., Bourdin, B., 2016. A variational hydraulic fracturing model coupled to a reservoir simulator. *Int. J. Rock Mech. Min. Sci.* 88, 137–150.
- Zhou, X., Burbey, T.J., 2014. Fluid effect on hydraulic fracture propagation behavior: a comparison between water and supercritical CO<sub>2</sub>-like fluid. *Geofluids* 14 (2), 174–188.
- Zhu, W., Wei, C., Li, S., Wei, J., Zhang, M., 2013. Numerical modeling on destress blasting in coal seam for enhancing gas drainage. *Int. J. Rock Mech. Min. Sci.* 59, 179–190.